UNIVERSITY OF OKLAHOMA

GRADUATE COLLEGE

ADDITIVE MANUFACTURING OF POLYDIMETHYLSILOXANE (PDMS)/CARBON NANOTUBE (CNT) NANOCOMPOSITE SENSORS

A THESIS

SUBMITTED TO THE GRADUATE FACULTY

in partial fulfillment of the requirements for the

Degree of

MASTER OF SCIENCE

By

MOHAMMAD CHARARA
Norman, Oklahoma
2019

ADDITIVE MANUFACTURING OF POLYDIMETHYLSILOXANE (PDMS)/CARBON NANOTUBE (CNT) NANOCOMPOSITE SENSORS

A THESIS APPROVED FOR THE
SCHOOL OF AEROSPACE AND MECHANICAL ENGINEERING

BY

Dr. Mrinal C. Saha, Chair

Dr. Yingtao Liu, Co-Chair

Dr. M. Cengiz Altan

Acknowledgement

First and foremost, I would like to express my deepest gratitude to Professor Mrinal Saha at the University of Oklahoma (OU) for providing me with the opportunity to become involved in his research group and providing the guidance, environment, and creative freedom to facilitate my development as a researcher. In addition, I would like to thank Professor M. Cengiz Altan for his encouragement, insightful commentary, and thought-provoking ideas with regards to my research over the past 2 years. I believe I would not be at OU today if it were not for the encouragement and efforts of Professors Altan and Saha, and will be forever grateful to them for taking a chance on me and providing me with the opportunity to pursue my dreams in higher education. I would also like to thank Dr. Yingtao Liu, who's guidance, patience, creative ideas, encouragement, and constant reminders to think and plan for the future helped me accomplish many goals, set my aim for the stars, and understand how to navigate a future in academia.

My time at OU would not have been possible without those in my personal life. I want to thank my lab mates, Wenyuan Luo, Anirban Mondal, Musa Sukati, and Nelson Barrios Rodriguez, who helped me navigate new fields when I first joined and granted me the opportunity to mentor and share the knowledge and topics I am passionate about. I want to thank my close friends Mohammad Abshirini, Parisa Marashizadeh, Ben Hoelzel, and Blake Herren. Their support and friendship made the last two years a pleasure, even on the hardest days. In addition, my close friends Mehrad Amirkhosravi and Maya Pishvar have been instrumental in providing invaluable advice and comments on my work, helping me to understand life in academia on a deeper level through our daily interactions as they navigate a post-doctoral life.

I recognize that I would not be where I am today if it were not for my family. The hard work and sacrifices of my parents, Talal and Wafaa Charara, have made this pursuit possible for

me, as I would not be in a position to do so without their decision to move to the USA. I want to thank my sisters, Abir and Zahraa Charara for their encouragement and constant support regardless of the task. I want to thank my girlfriend, Laura Pratt, whose love and support have made Norman a home for me. I would also like to thank Tom and Marsha Pratt, who have helped support Laura and me ceaselessly through our academic endeavors.

Lastly, I want to thank the wonderful staff at the School of Aerospace and Mechanical Engineering at OU: Bethany Burklund, Martina Ferguson, Melissa Foster, Ellen McKenzie, Rebeka Morales, Billy Mays, and Greg Williams. I have appreciated their support, advice, and friendship through my time at OU and believe they keep the school running like a well-oiled machine!

Dedication

I want to dedicate this thesis to my parents, Talal and Wafaa Charara, who taught me the value to continually pursuing education and whose sacrifices and persistence granted me the opportunity to do so. I also want to dedicate this thesis to my girlfriend, Laura Pratt, whose love and dedication have motivated me to continue to work hard, even in the roughest times.

Table of Contents

Acknowledgement 4

Dedication 6

Table of Figures 10

Table of Tables 13

Abstract 14

CHAPTER 1. INTRODUCTION 1

1.1. Elastomer Based Multifunctional Nanocomposites 2

1.1.1. CB 6

1.1.2. Graphene 8

1.1.3. CNT 9

1.2. PDMS Sensor Manufacturing Techniques 11

1.2.1. 3D printing of PDMS 13

1.3. Scope of Work 15

1.4. Research objective 16

CHAPTER 2. EXPLORATION OF PDMS/CNT INK 18

2.1. Introduction 18

2.2. Experimental 18

2.2.1. Materials 18

2.2.2. Nanocomposite Synthesis 18

2.2.3. Rheology 19
2.2.4. 3D printing 20
2.2.5. Cast Sample Fabrication 22
2.2.6. Porosity measurements 22
2.2.7. Resistivity/Conductivity Measurements 23
2.3. Results 24
2.3.1. Rheology 24
2.3.2. 3D Printing 26
2.3.3. Porosity 27
2.3.4. Resistivity/Conductivity Measurements 34
2.4. Conclusion 36
CHAPTER 3. OPTIMIZATION OF 3D PRINTING PARAMETERS 37
3.1. Introduction 37
3.2. Experimental 37
3.2.1. Cyclic Piezoresistive Testing 37
3.3. Results 39
3.3.1. Isotropy Test 39
3.3.2. Piezoresistive Behavior – 3D Printed vs Cast 43
3.3.3. 3D Printing Parameters 47
3.4. Conclusion 53

CHAPTER 4. PIEZORESISTIVE SENSOR CHARACTERIZATION 55

4.1. Introduction 55

4.2. Experimental 55

4.2.1. Characterization of piezoresistive sensors under cyclic compressive loads 55

4.2.2. Characterization of piezoresistive sensing mechanism 56

4.3. Results 57

4.3.1. Microscale morphology of MWCNTs in nanocomposites 57

4.3.2. Piezoresistive sensing under compressive loads 58

4.3.3. Characterization of piezoresistive sensing mechanism 67

4.4. Conclusion 69

CHAPTER 5. CONCLUSION AND FUTURE WORK 70

REFERENCES 74

Table of Figures

Figure 1. Elastomer's change in geometry due to mechanical deformation (not to scale)..... 3

Figure 2. CNT network rearrangement as a result of compression (not to scale). 5

Figure 3. Tunneling effect 3D resistor network model visualized (R_{tunnel}: tunneling resistance, R_{cn}: resistance of a single CNT) [14]..... 5

Figure 4. Stress vs. strain and $\Delta R/R$ vs strain curves (King et al.)[16]..... 8

Figure 5. Resistivity percolation curve of 3 different types of CNTs (Pegel et al.) [28]..... 11

Figure 6. Schematic of PDMS/CNT nanocomposite ink synthesis, and 3D printing [49]. 20

Figure 7. Layer by layer 3D printing of free standing PDMS/CNT [49]. 21

Figure 8. Sliced 3D printed patterns - (a) concentric and (b) rectilinear. 21

Figure 9. Mold used to create cast samples. 22

Figure 10. Amplitude sweep rheology test results for PDMS/CNT inks with 1.0 to 3.0 wt% CNT content..... 25

Figure 11. Trimetric views of the resulting 3D printed cubes from (a) rectilinear and (b) concentric patterns. 26

Figure 12. X-Z in-plane view of the (a) rectilinear and (b) concentric 3D printed cubes. 26

Figure 13. Cross section of 3D printed samples using the (a) rectilinear and (b) concentric printing patterns. 27

Figure 14. Porosity of 3D printed parts using the rectilinear and concentric printing patterns for PDMS/CNT nanocomposites with 1.5 to 3.0 wt% CNT loading. 29

Figure 15. Low magnification (low mag) SEM Images of pores within 3D printed 3.0 wt% CNT content nanocomposites manufactured with the (a) rectiliinear and (b) concentric printing

patterns. The dashed arrows in each image represent the printing direction, coincident with the bissection direction. 31
Figure 16. (a) low and (b) high mag SEM images of 3D printed 1.5 wt% CNT content nanocomposites manufactured with the rectilinear 3D printing pattern. 32
Figure 17. (a, b, d) High and (c) low mag SEM images of 3D printed 1.5 wt% CNT content nanocomposites manufactured with the concentric 3D printing pattern. 32
Figure 18. Layer by layer 3D printing process – filamentary extrusion is dragged across printing surface rather than deposited. 33
Figure 19. Examples of voids created while 3D printing with the 3.0 wt% CNT PDMS/CNT nanocomposite ink. 33
Figure 20. Resistivity and Conductivity for 3D printed and cast samples of different wt% CNT concentrations. 35
Figure 21. Test setup for cyclic piezoresistive testing [49]. 39
Figure 22. Isotropy study comparing the piezoresistive response of the printed PDMS/CNT nanocomposite in all 3 axes for the (a) concentric and (b) rectilinear 3D printing patterns..... 41
Figure 23. Compressive Young's Modulus in the X, Y, and Z axes for printed PDMS/CNT ink nanocomposite with 1.5 wt% CNT content – (a) concentric and (b) rectilinear 3D printing patterns. 42
Figure 24. Piezoresistive response of cast, sensors compared to 3D printed counterparts..... 44
Figure 25. Mechanical response of cast, sensors compared to 3D printed counterparts. 45
Figure 26. (a) Widely understood nozzle induced nanofiller alignment; (b) nanofiller alignment post-deposition; (c) nanofiller de-alignment due to interactions between adjacent layers. 50

Figure 27. (a) Comparison of shear induced alignment in small and large nozzles; (b) CNT de-alignment due to interactions between adjacent layers (large nozzle). 51
Figure 28. 3D printing parameter effect – cyclic piezoresistance test results for (a) variation for printing speed and (b) variation of nozzle size. 52
Figure 29. Experimental setup for in situ micro-strain testing SEM imaging [49]. 57
Figure 30. SEM images of PDMS/MWCNT compression sensor cross-section at four locations (magnification of 28803 in (a) and (c), and magnification of 20003 in (b) and (d)). 58
Figure 31. Cyclic strain testing at various max strains, holding crosshead speed constant: (a) relative resistance change versus cycle count and (b) applied strain versus cycle count. 60
Figure 32. (a) Gauge factor and (b) ΔR/R versus strain based on cyclic loading at various max strains. 62
Figure 33(a) Stress vs strain and (b)ΔR/R vs strain for the 3D printed sensor. 63
Figure 34. Relative resistance change results for cyclic loading at varying strain rates – (a) cyclic and (b) summarized results. 65
Figure 35. Relative resistance change for (a) the durability test and (b) 5 representative cycles at various phases in the test 66
Figure 36. Stress versus strain curve at 3 representative cycles of the durability test. 67
Figure 37. SEM images of in situ micromechanical tests before (a) and after (b) application of compressive load. 68

Table of Tables

Table 1. Yield point values extracted from the rheological oscillatory test. 25

Table 2. Samples printed and tested (piezoresistivity). 38

Table 3. Young's Modulus values in the X, Y, and Z axes for printed PDMS/CNT nanocomposite. 43

Table 4. Print times for samples printed at varying print speeds – concentric printing pattern. .. 48

Table 5. Print times for samples printed at varying nozzle sizes – concentric printing pattern. .. 49

Abstract

Highly elastic nanocomposite strain sensors have recently received considerable attention in academic research due to broad applications in fields, such as biomedical and robotics. These sensors combine flexible polymers, like polydimethylsiloxane (PDMS), and nanofillers, like carbon nanotubes (CNTs), to increase the electrical conductivity of the base polymer. Typically, these nanocomposites exhibit a change in mechanical property in response to mechanical stimulus, allowing researchers to correlate mechanical deformation to a change in electrical properties. These sensors, however, are often made using methods that are time consuming, waste substantial amounts of material, and require expensive equipment, such as lithography and casting. To address these issues with current sensor manufacturing technology, in this thesis I present 3D printing as a viable alternative to other nanocomposite sensor manufacturing techniques.

To 3D print bulk structures, the extruded materials must have a yield point, so that it can maintain its own weight, and the weight of all layers above it, after printing while curing. Because PDMS does not possess a yield point in its pristine state, CNT's were added to the material to serve as a thixotropic agent and electrical filler. Rheological testing, via amplitude sweeps, on PDMS/CNT formulations between 1.0 and 3.0 wt% CNT revealed that all formulations with CNT wt% at or above 1.5 possessed a yield point and could be 3D printed. 3D printed cubes were created from the nanocomposite inks with a yield point using two distinct printing patterns. Comparing their electrical properties to that of the cast material, tests revealed that the PDMS/CNT formulation of 1.5 wt% was the ideal formulation and that the 3D printed samples showed a similar conductivity curve as the cast samples.

To test the effect of 3D printing parameters on the piezoresistive response PDMS/CNT compression sensors, samples were 3D printed using various 3D printing needle sizes, various 3D

printing speeds, and various infill techniques. The tests reveal that the sample display isotropic piezoresistive behavior which is not dependent on printing speed or 3D printing needle size.

Using this information, a 3D printed sensor was fully characterized using cyclic testing at various max strains and various strain rates. The results reveal the sensor's resistance increases with applied strain and is highly sensitive, with gauge factors as high as 24 at strains of 1%. Moreover, the sensor displays versatile piezoresistive response with little to no change at varying strain rates. The sensor's robustness is tested via a 500-cycle durability test which revealed minimal electrical and mechanical degradation from the first to last cycle. Lastly, in-situ micromechanical compressive tests under scanning electron microscope validated the sensor's piezoresistive mechanism, showing the CNT network rearrangement under compressive load.

This work proves the viability of fabricating nanocomposite-based compression sensors via 3D printing rather than cast. The isotropic behavior of the printed sensors can be exploited to 3D print complex geometries using various 3D printing patterns to achieve similar results to cast sensors without the need for molds.

CHAPTER 1. INTRODUCTION

Nanocomposite flexible sensors have attracted a great deal of attention in the research community due to their application in a vast array of fields, such as such as robotics [1], structural health monitoring [2], and biomedical [3]. Traditional sensors, such as the conventional foil strain gauge, are typically employed for these tasks and are commercially available. However, these sensors have a limited sensing range (about 5% strain) and low sensitivity [4]. Nanocomposite strain sensors are a viable alternative, as they offer tunable stretch ability and sensitivity, depending on their constituents. The higher strain that these sensors can register may be useful in the medical field as joint motion sensors, for example, where physical therapists can quantify a patent's motion based on the sensor's response and asses the patient's progress to create a regiment for rehabilitation.

Nanocomposites for strain sensing applications have been synthesized using a variety of matrices, such thermosets, thermoplastics, and elastomers, and nanofillers, such as carbon black (CB), graphite, and carbon nanotubes (CNTs) [5]. Of these matrices, the elastomer polydimethylsiloxane (PDMS), also known as dimethicone, has gathered significant attention due its chemical inertness, flexibility, and biocompatibility for its potential use in biomedical applications. In addition, its low cost and optical transparency has made it popular in other fields, such as microfluidics [6].

In the context of strain sensors, however, one of the more studied characteristics of PDMS has been its mechanical properties, which are highly tunable depending on the polymer constituent ratio and processing parameters. Although PDMS comes in a variety of formulations from various manufacturers, one of the most common found in literature is Sylgard 184. This PDMS formulation comes in the form of a liquid base prepolymer (part A) that needs to be mixed with a

copolymer/catalyst solution (part B) in order to initiate the polymerization reaction. Leveraging the mixing ratio of these polymers, researchers have investigated increasing and decreasing the 10:1 part A to part B manufacturer recommended mixing ratio to study its effects on mechanical properties. These studies revealed that an increase in the mechanical properties was found with an increase in catalyst content (increase in part B) [7], while suffering a decrease in stretch ability [8]. In addition, further studies have been carried out to study the effect of PDMS curing temperature on its mechanical properties. Like catalyst content, an increase in the curing temperature was found to increase the material's mechanical properties [9]. This mechanical property tunability becomes advantageous when designing a material for sensing applications, where one application may require a material with higher compliance than another. Moreover, the relative ease with which the mechanical properties can be customized makes PDMS a highly attractive polymer to use as a matrix for a strain sensor.

1.1. Elastomer Based Multifunctional Nanocomposites

Although PDMS is a great candidate for use in strain sensing applications, in its pristine form, the polymer does not possess the commonly used material properties which can be exploited for sensing purposes. Typically, elastomers like PDMS must first be mixed with nanofillers to enhance their electrical conductivity. These elastomers can then be used as sensors by monitoring the change in various electrical properties under a mechanical stimulus. Researchers have previously proved this concept, showing changes in a nanocomposite sample's electric capacitance [10] and resistance [11, 12] as a result of strain.

Of these various sensing modes, a material's change in resistance, or piezoresistive, has garnered considerable attention. The piezoresistive mechanism is due to a combination of factors. First, it is important to note that highly stretchable elastomers typically possess high Poisson's

ratios, or ratios of lateral deformation as a response to longitudinal deformation (PDMS for example has a Poisson's ratio of about 0.4). We can see the effect of this material property by studying the equations for electrical resistance and conductivity (Eq. 1),

$$R = \rho \frac{l}{A} \quad (1)$$

$$\sigma = \frac{1}{\rho} \quad (2)$$

where R is a sample's electrical resistance, ρ is the material's electrical resistivity, l is the samples length along the direction tested, A is the cross section of the sample on the plane perpendicular to the direction tested, and σ is the sample's electrical conductivity. Moreover, Figure 1 helps to visualize the Poisson's ratio's effect on the geometry of the sample. As the sample's cross-sectional area increases due to compression, its resistance decreases, and conductivity increases. The opposite is true from a sample subjected to tension, as its cross section would decrease, and the length of the sample would increase.

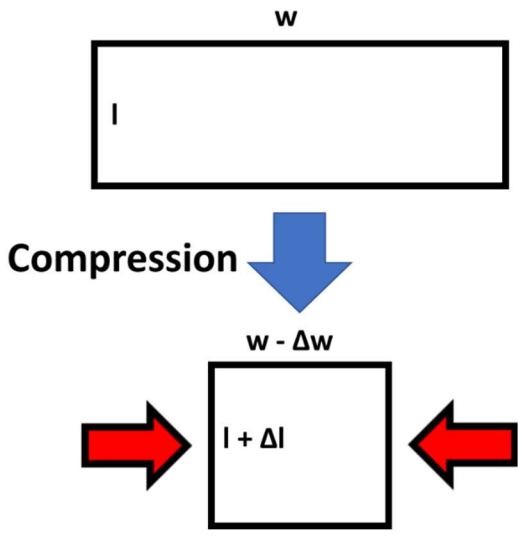

Figure 1. Elastomer's change in geometry due to mechanical deformation (not to scale).

In addition, the inclusion of fillers adds another mechanism for resistance change due to interactions between each individual filler particle during material stretching and compression. Figure 2 shows an example of an elastomer-based CNT-doped nanocomposite being subjected to compression (laterally), where the white area represents the polymer matrix and the black lines represent CNT fillers. CNTs are used here as an example, but as previously mentioned, other fillers can also be used to achieve this effect. As the material is compressed, the CNTs act as an incompressible material, so the mechanical compression causes them to move, rotate, and bend. As they move and get closer to each other, nanotubes that were previously too far to conduct from one another begin to form electrical networks. Because the resistance of the CNTs is much higher than that of the elastomer matrix, as the CNTs get closer, the conductivity of the material changes. Electron tunneling is widely considered to be the main cause of this.

As previously mentioned, when nanotubes are too far away from each other, electron transfer does not occur, and thus electrical conductivity is not present. As CNTs are brought close together due to material deformation, they reach a critical inter-filler distance at which the electron from one of the nanotubes can overcome the resistance of the matrix to jump from one CNT to the other. This is called the tunneling distance [13, 14]. As this tunneling distance is achieved for more and more networks, the resistance of the nanocomposite decreases. This results in a mechanism that can be exploited to relate to changes in material geometry to changes in resistance, and thus they can be used as sensors. It should be noted that this piezoresistive tunneling effect is also true in tension, where the material is being stretched and CNT networks are being broken as they distance between CNTs increases past the tunneling distance, thereby increasing the nanocomposite's electrical resistance. Typically, studies discussing computational techniques simulating piezoresistive effects of nanoparticles within an insulating matrix translate this tunneling effect

into an analogous resistance model, where CNTs are assigned an electrical resistance value and the resistance between particles is given a value based on their proximity (Figure 3 [14]). This phenomenon is not explained in detail in this body of work, but is thoroughly explained in Hu et al.'s computational efforts [14].

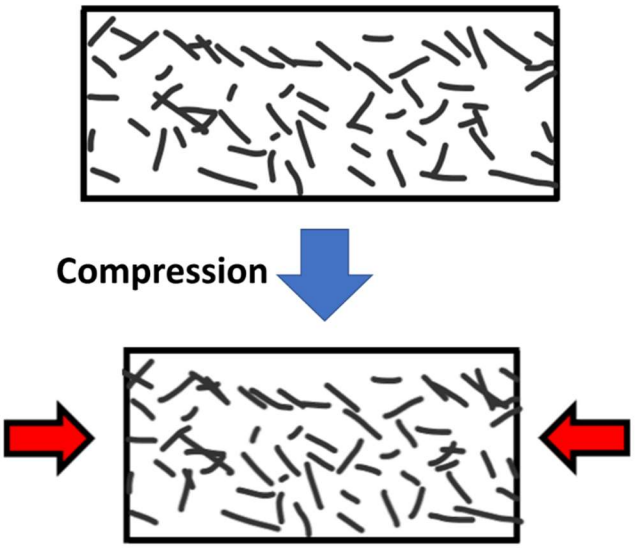

Figure 2. CNT network rearrangement as a result of compression (not to scale).

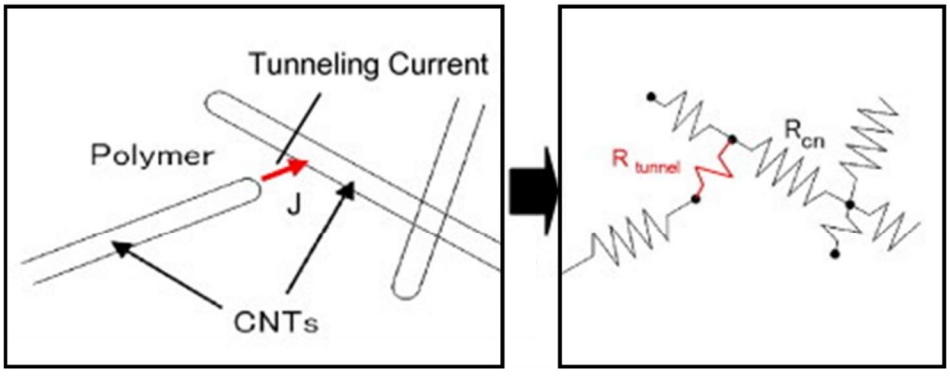

Figure 3. Tunneling effect 3D resistor network model visualized (R_{tunnel}: tunneling resistance, R_{cn}: resistance of a single CNT) [14].

Although sensor elasticity/flexibility is one important factor, once the polymer matrix has been doped with nanoparticles to create a multifunctional nanocomposite, an important feature to consider is sensor sensitivity. A common wat to quantify the resistance response sensitivity of piezoresistive nanocomposites under strain is the Gauge Factor (GF). This is defined as the relative resistance change of a sensor normalized by the applied strain. Equations 3, 4, and 5 below show the definitions of strain (ε), relative resistance change ($\Delta R/R$), and GF

$$\varepsilon = \frac{l - \Delta l}{l} \quad (3)$$

$$\Delta R/R = \frac{R - R_o}{R_o} \quad (4)$$

$$GF = \frac{\Delta R/R}{\varepsilon} \quad (5)$$

where, l is the original length of the sample along the axis of deformation, Δl is the change in the length of the sample due to deformation, R is the resistance of the sample at a particular point during a deformation test, and R_o is the original resistance of the sample.

Various nanofillers have been used to take advantage of this effect and provide additional mechanisms for resistance change. The following is a brief summary the use of CB, graphene, and CNTs in nanocomposite strain sensors.

1.1.1. CB

Carbon black is a spherical nanoparticle created as a biproduct during petroleum combustion. Typically, CB is used in the manufacturing of car tires. However, the addition of CB into an insulating elastomeric matrix has been shown to induce piezoresistive characteristics in the matrix polymer. Several studies have explored this phenomenon. Luheng et al., for example, created a

silicone rubber/CB nanocomposite of various CB content to explore the effects of nanofiller content on the piezoresistive response of the material. Testing various CB to silicone rubber ratios between 0.08:1 and 0.24:1, they found that for different ratios, not only was the piezoresistive response of the material different, but the piezoresistive mechanism changed. At lower CB content, the resistance of the sample increased with the application of pressure, while at higher CB contents (> 0.16:1), the resistance decreased. As the CB content increased to the highest ratios, the piezoresistive effect was dampened by the reduction of resistance as a result of increased conductive paths available, resulting in reduced $\Delta R/R$ [15]. The same research group later explored the this change in piezoresistive behavior (decreasing vs. increasing resistance under pressure) and proved that they could identify a critical pressure whereby the resistance changed from decreasing to increasing. Studying the same silicone rubber/CB material, they found that as the CB content changed, so did this critical pressure [15]. What we can conclude from these sets of studies is that although the inclusion of CB endows a material with piezoresistive properties, this resistance change response may not be predictable. In addition, the relatively low resistance change of the material at its most sensitive formulation (0.16:1 CB to silicone rubber with $\Delta R/R$=~40%) was achieved at pressures of 1 MPa, showing that this material may not be suitable for highly sensitive sensors.

Other researchers have shown the use of CB in nanocomposites can achieve consistently sensitive results over a large sensing range. King et al., for example, developed a porous PDMS/CB-based nanocomposite and tested its piezoresistive response over a compression strain range between 0 and 95% [16]. The stress-strain and $\Delta R/R$ vs strain curves are shown in Figure 4. Although the resistance change vs strain curve shows an almost linear relationship between the two, the sensing range is relatively small, with the maximum sensing pressure of 0.14 MPa. It is

worth noting that to achieve this linear sensing relationship, the authors generated porous PDMS, which requires substantial amount of time to manufacture, and the CB deposited in the PDMS scaffold cannot be quantified, resulting in possibly inconsistent content from sample to sample.

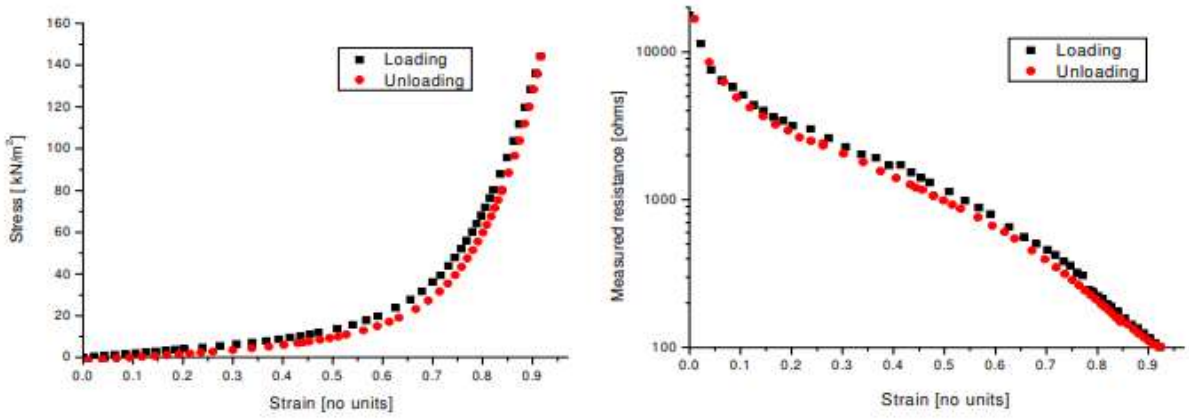

Figure 4. Stress vs. strain and ΔR/R vs strain curves (King et al.)[16].

Finally, the largest detractor of the use of CB in pressure and strain sensors is its relatively low conductivity compared to other fillers. Studies report that CB content between 10% and 50% is required to achieve a repeatable sensing response with adequate sensitivity [4, 17, 18]. This high filler content has the potential of altering the mechanical characteristics of the base polymer and hinder its elasticity. For this reason, although CB is relatively cheap compared to other nanofillers, researchers have sought alternatives to CB to include in piezoresistive nanocomposites.

1.1.2. Graphene

Graphene, first discovered in 2004 [19], is a 2D planar nanoparticle composed of a single layer of hexagonally bonded carbon atoms. Recently, researchers have taken great interest in exploring the use of graphene as fillers in pressure and strain sensor. Yao et al. conducted a study by which they fabricated a polyurethane sponge and doped it with graphene-based fillers. The resulting was a highly sensitive pressure sensor that could detect pressures as low as 9 Pa [20].

Although highly sensitive, these sensors were only tested to 25 Pa, limiting their sensing range and applications. Sheng et al. created a graphene-oxide (GO) film and tested it at much higher strains (~50%) to find that the sensor showed high sensitivity ($^{\Delta R}/_{R}$ = 80%) between 0-10% strain, but relatively low resistance change thereafter. Although the sensor fabricated in this study had a higher maximum tested pressure than the previous study, the 10 kPa it was tested at shows a limitation in its sensing range. Other studies support these claims [21, 22]. Although these sensors have been tested to pressures as high as 20 kPa, the range of highest sensitivity with graphene-based nanocomposites lies below 10 kPa.

Studies with graphene show its utility in piezoresistive compression sensors. Moreover, the sensitivity is much higher than that found with CB. The biggest drawbacks to using graphene are its price and dispersion. Graphene nanoparticles are not cheap, and may cost as high as $175 for 500 mg. This makes it extremely difficult to conduct exploratory research that requires large quantities of nanomaterials. Moreover, because graphene's large surface area, it's surface energy and Van der Waals forces cause individual graphene sheets to stack together, creating difficulties when dispersing [23]. This becomes an issue because if too much energy is input into a system while sonicating, the sheets may be fractured, but if not enough energy in input, the sheets will not separate. Poor dispersion significantly lowers the potential effect that graphene can have on a matrix's electrical and mechanical properties.

1.1.3. CNT

Since their discovery in 1991 by Ijima et al. [24], CNTs have become a highly popular nanofiller, used in many fields of research to improve a material's electrical and mechanical properties, among others. As such, numerous studies have been conducted exploring the effect of CNTs on a material's piezoresistive properties. Abshirini et al., for example, generated a

PDMS/CNT strain gauge that shows excellent repeatable response to applied tensile strain, with a *GF* of about 4.3 [12]. In this experiment, however, the CNT amount in the nanocomposite section of the sensor was not quantified. Hu et al. performed a computational study of an epoxy/CNT polymer's piezoresistive response in tensile and compressive loads and validated these results with experiments [25]. In addition, they studied how processing parameters, such as curing temperature, affected the sensor's sensitivity. They were able to obtain sensors with a *GF* of about 22.5. This large difference between the *GF* attained in the 2 different studies is likely due to the matrix used for the sensor. Stiffer materials, such as epoxies, tend to produce strain sensors with higher gauge factors. This may be because the strain is largely limited, affecting the internal network rearrangement of the nanofillers within the matrix. Numerous other studies have also explored the use of CNTs as electrically conductive fillers in piezoresistive nanocomposites [26, 27].

The main reason for CNT's popularity in piezoresistive sensing applications is its high conductivity. In nanocomposites, the minimum amount of filler that endows the matrix with electrical conductivity is referred to as the percolation threshold. As the filler content increases from the percolation threshold, the conductivity of the nanocomposite increases (resistivity decreases) until an asymptote is reached where the electrical networks have saturated. Figure 5 shows the percolation curves for 3 different types of CNTs as an example [28]. Two of the types of CNTs shown in the figure display typical percolation behavior, where a critical concentration of filler (in this case CNT) is reached resulting in a rapid drop in resistivity until some sort of electrical saturation is reached. This percolation threshold is highly dependent on the geometry of the filler, with aspect ratio (AR) being one of the deciding factors. This is what makes CNTs ideal as electrically conducting fillers. CNT's are synthesized in a wide array of ARs, but typically those with a larger AR will reach percolation at lower content [29]. If CNTs are laid end to end, fewer

CNTs will be required to conduct electricity from one side of a sample to the other if the CNTs are longer. Because CNTs come in a wide array of ARs, the percolation ratio can be tuned to also exploit CNT's mechanical properties.

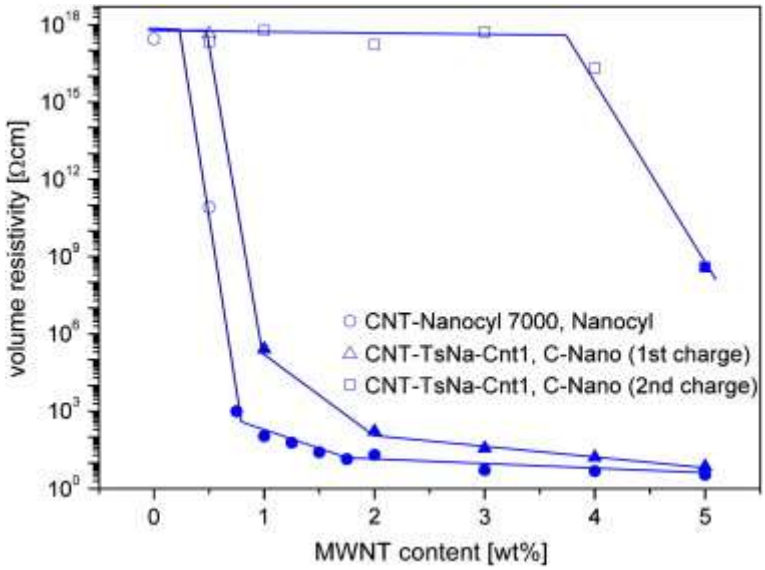

Figure 5. Resistivity percolation curve of 3 different types of CNTs (Pegel et al.) [28].

In this study, CNTs were used as the conductive filler for these very reasons. Although graphene has been shown to achieve excellent piezoresistive properties at low material content, CNTs are much cheaper and can reach percolation at comparable content. In addition, although CB is much cheaper than CNT, the high percolation threshold means that the mechanical and rheological properties of the matrix material may be altered significantly due to the large content of stiff filler [29, 30]. This is an imperative detail in flexible strain/compression sensors as it can diminish the elasticity of the matrix material used.

1.2. PDMS Sensor Manufacturing Techniques

Elastomer-based sensors have been manufactured in several ways. PDMS-based sensors in particular have been manufactured using lithography [31], templating [32, 33], cast molding [34],

and additive manufacturing [35]. Compared to additive manufacturing, conventional nanocomposite manufacturing typically employs the use of molds, which are time consuming to create and wasteful to manufacture. In addition, lithography can be a time consuming iterative process (depending on how many PDMS layers will be required for the final sample), requiring expensive equipment to etch away material not covered by a photoresist [36]. Additive manufacturing, or 3D printing, on the other hand, is a vastly simple customizable process.

There are various 3D printing techniques available, including stereolithography, selective laser sintering (SLS), and fused filament fabrication (FFF) (also known as fused deposition modeling (FDM), but that term has since been trademarked by the 3D printer manufacturer Sratasys). Of these, FFF 3D printers are most commonly available. In this technique 2D prints are successively printed on top of each other to create a 3D geometry. The desired geometry is generated using a computer aided design (CAD) software, such as Solidworks, and converted into a gcode file that the 3D printer can translate to printing instructions by a slicing software, such as Slic3r. The slicing software takes into account various parameters set by the user, such as nozzle diameter, desired layer heights, and printing speed, to divide the geometry into a set of stacked 2D cross sections which are further divided into lines serving as paths for the nozzle to deposit the desired 3D printed material. This fabrication method is highly popular with thermoplastic materials, such as acrylonitrile butadiene styrene (ABS) [37, 38], polylactic acid (PLA) [39], and polyamide [40]. Increasingly, this technology has been employed, with some modification, to 3D print pristine and functional elastomer-based nanocomposite materials, also referred to as functional inks [35, 41-45]. More specifically, in the context of this work, this technology has been used for the 3D printing of PDMS, PDMS based polymeric formulations, and PDMS based

nanocomposites [35, 41, 43]. In the next section, a short summary of current PDMS 3D printing efforts will be presented.

1.2.1. 3D printing of PDMS

Additive manufacturing of PDMS has drawn a great deal of attention over the past decade. The current 3D printing revolution has motivated researchers to print many nonconventional materials. In the case of PDMS, numerous applications, such as microfluidics devices [46] and strain sensors [47], have largely benefitted as a result.

The main issue with 3D printing PDMS is its rheological properties. At room temperature, PDMS does not possess a yield point. This means that if it is being used as a 3D printable material, the deposited polymer will wet the surface immediately after deposition. Not only does this make it impossible to stack multiple layers of pristine PDMS material vertically, even layers printed on plane will lose their fidelity due to surface wetting. To tackle this issue, researchers have employed various techniques, including using a support bath, using embedded printing, and mixing the pristine polymer with a thixotropic agent. The next sub sections briefly describe and digest each method.

1.2.1.1. Support bath

To overcome yield point issues, Hinton et al. employed the use of a support bath [41]. In this method, a bath made from a material with a yield point is used to support the 3D printed PDMS and prevent it from flowing before and during curing. The 3D printing setup this group used was a syringe-based extruder capped with a needle. The researchers chose various types of Carbopol, a water-soluble polymer that can be used to create a hydrogel, to compare which one yielded prints with highest fidelity. The outcome of this study was the successful 3D printing of PDMS shell

structures. However, this study was not able to produce a solid structure, only shell structures. Due to Carbopol's relatively high yield point, as the depositing needle translated through the support gel, it left a cavity in the support bath. The yield point was high enough to prevent the Carbopol polymer to flowing together immediately after the needles passed, closing the path left behind. In return, because there was pressure being applied from the Carbopol bath onto the deposited PDMS, the PDMS flowed up the cavity walls. Although this extra pressure proved useful in bonding vertical layers (layers from the bottom were forced to bond with those above), it proved problematic when attempting to fuse lateral layers, as required for a solid print. This along with other nonuniform stresses within the Carbopol bath made the printing of solid structure unsuccessful. Other attempts at printing PDMS, like Bhattacharjee et al., showed similar results, although the authors did not discuss the resulting shell structures thoroughly [48].

1.2.1.2. Embedded printing

To circumvent rheological issues with the support bath, Muth et al. employed the use of a filler fluid to prevent deposited material from flowing up through a cavity [35]. In this study, an elastomeric reservoir is used for support while a carbon grease solution (typically made from PDMS and CB) is printed within. To avoid forming a void after the needle passed through the support bath, the researchers used a low viscosity filler fluid which would immediately fill the cavity created by the needle, thereby preventing the deposited fluid to push up the cavity walls. This method proved successful in creating 3D printed embedded strain sensors on a 2D plane.

Recently, a new study has explored the expansion of embedded printing into 3D vertical prints. With the goal of using a support bath print, Grosskopf et al. explored mixing SE 1700, fumed silica nanoparticles used as a thixotropic agent, with PDMS. The highlight of this work is that the researchers explored supports baths with various PDMS and SE 1700 to optimize a bath with the

correct rheological properties for the printed Pluronic F127-based ink formulation. This study could be used as a model to optimize a support bath to print materials with other rheological properties.

Although both studies proved successful in embedded 3D printing, the goal of this work is to 3D print a PDMS based nanocomposite without the use of supporting materials, much like thermoplastic 3D printing.

1.2.1.3. Thixotropic agent

Researchers have also explored way to deposit PDMS using a layer by layer method on an unsupported print bed. Ozbolat et al. used the same SE 1700 thixotropic agent to modify the rheology of the pristine PDMS polymer to print various structures [43]. Unlike Grosskopf et al., Ozbolat et al. modified the rheology of the printed materials rather than an embedding material [43, 45]. After exploring various SE 1700/PDMS formulations to tune the rheological properties of the printed polymer, the researchers successfully printed various simple and complex free-standing structures, such as a scale human nose and hand. Although this study follows the direction of the current work, the printed structures do not possess sensing capabilities as they do not have conductive fillers.

1.3. Scope of Work

In summary, nanocomposite strain and compression sensors have many potential applications. Although many elastomers have been used as matrices for these types of sensors, PDMS shows great promise due to its biocompatibility, high flexibility, and chemical inertness. Moreover, from the various types of fillers previously used, CNT has been shown to have potential for use in nanocomposite sensors due to its high conductivity and relatively low content to achieve electrical

percolation in a matrix. Nanocomposite sensors have been manufactured in numerous ways, but the method allowing for highest customization with lowest material and tooling potential cost is 3D printing, allowing users to bring virtually any computer-generated shape to life.

The challenge this work will tackle is adapting a PDMS/CNT nanocomposite formulation for free-standing 3D printing, like the popular FFF 3D printing method. These formulations are often referred to as nanocomposite inks. The literature review in this chapter discussed several methods researchers have used to 3D print PDMS-based ink. The method this work aims to emulate is the thixotropic agent method. However, rather than using a silicon-based thixotropic agent, CNTs will be used to tune the rheology of the PDMS/CNT nanocomposite to achieve a formulation that can bear its own weight prior to curing. The CNT content of this ink will be optimized to balance achieving a yield point and maximizing the ink's piezoresistive response. The 3D printed material's electrical and mechanical properties will be characterized and compared to its cast counterpart to prove that 3D printing is a viable alternative to casting, without compromising with the loss of sensing potential.

1.4. Research objective

The research objective of this work are as follows:

i. Synthesize a PDMS based nanocomposite ink with CNT that allows for free standing 3D printing
    a. Material must possess yield strength
    b. Material must use the minimum amount of CNT filler to maximize piezoresistive response
ii. Compare the piezoresistive performance of the printed material with cast

iii. Explore the effect of 3D printing parameters on the piezoresistive performance of the sensors

iv. Mechanical and electrical characterization of a 3D printed sensor

v. Understanding the piezoresistive sensing mechanism

CHAPTER 2. EXPLORATION OF PDMS/CNT INK

2.1. Introduction

This chapter discusses material preparation and filler content optimization with the goal of selecting a single nanocomposite ink to use for sensor additive manufacturing. For these purposes, the material must possess a yield point so that once deposited by the nozzle, it maintains its shape at deposition and does not fully wet the surface. In addition, it must contain the lowest possible CNT content while maintaining conductivity. This will place the material at a point on the percolation curve such that the electrical response to the application of mechanical compression will be maximized. Both the rheological and electrical properties of the material will be tailored using CNTs. For reference, this chapter addresses research objective (i.a.) and (i.b.), mentioned in section 1.4 Research objective.

2.2. Experimental

2.2.1. Materials

All materials were used as received unless otherwise noted. Sylgard 184 PDMS was acquired from Dow Corning. The PDMS polymer was composed of a prepolymer (part A) and a catalyst (part B), used to initiate and accelerate the polymerization reaction. CNTs with inner diameters of 50-90 nm and an aspect ratio of 100 were acquired from Sigma Aldrich. Tetrahydrofuran (THF), used as the dispersing solvent, was acquired from Sigma Aldrich.

2.2.2. Nanocomposite Synthesis

To develop a 3D printable nanocomposite ink, CNTs were first dispersed into the PDMS elastomer to create a PDMS/CNT nanocomposite. A predetermined amount of CNTs was added to a container with 40 mL of THF. In a separate container, a predetermined amount of part A

PDMS was added to a container with 30 mL of THF. The CNT/THF solution was magnetically stirred for 2 min at 350 revolutions per min (RPM) to wet the CNTs with THF, and then sonicated using a 750 W tip sonicator for 10 min at a pulse of 5s on/2 s off to further improve CNT dispersion. Meanwhile, the PDMS/THF solution was magnetically stirred at 350 RPM to reduce phase separation. Once the sonication of the CNT/THF solution was complete, it was poured into the PDMS/THF solution and the combined mixture was magnetically stirred for 2 minutes at 350 RPM. The PDMS/CNT/THF solution was then sonicated for 30 minutes using a 5 s on/2 s off pulse to disperse the CNTs into the PDMS matrix. Finally, the PDMS/CNT/THF solution was magnetically stirred on a hot plate at 350 RPM and 70 °C overnight to evaporate the THF. The resultant mixture produced a nanocomposite ink with apparent yield strength.

2.2.3. Rheology

To understand the viscoelastic properties of the uncured material, rheology experiments were performed to obtain the yield point values. A TA Instruments Discovery HR-2 rheometer equipped with a cone fixture was used for yield point measurements. The cone fixture had a 40 mm diameter and a cone angle of 2°. An amplitude sweep test was performed for PDMS/CNT inks containing 1.0 – 3.0 wt% CNT. The test gap was set to 53 μm for all experiments.

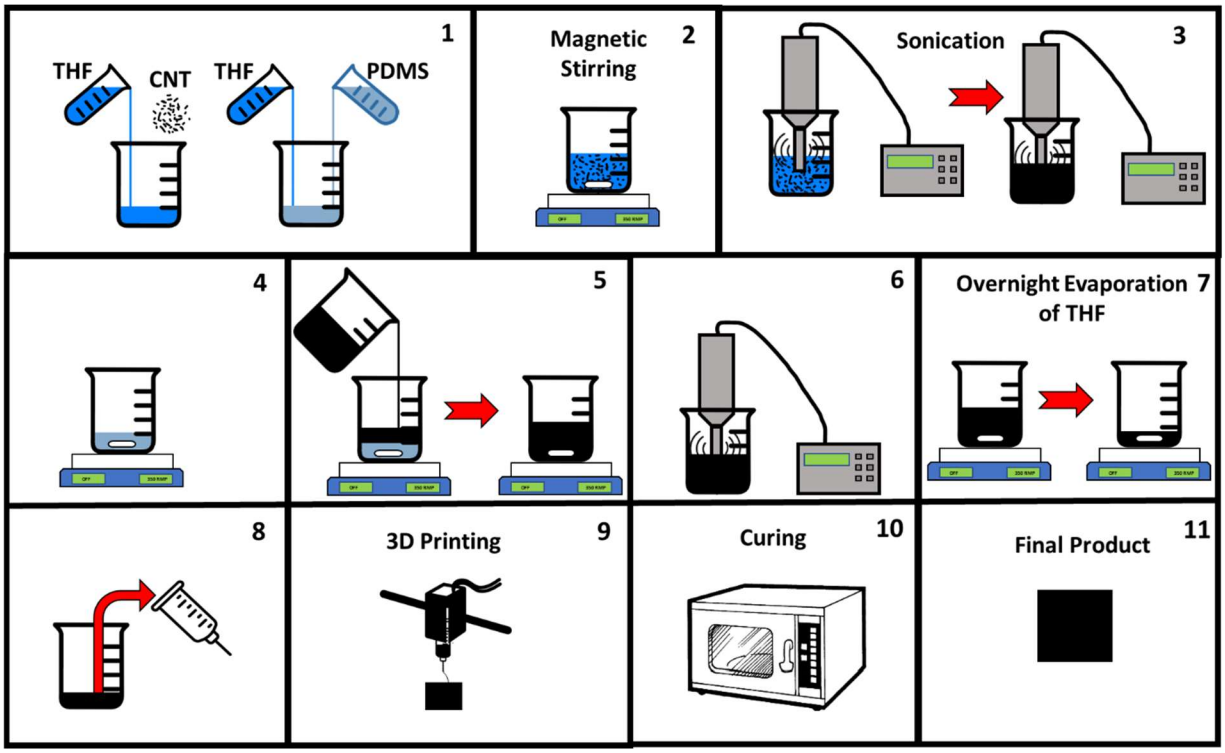

Figure 6. Schematic of PDMS/CNT nanocomposite ink synthesis, and 3D printing [49].

2.2.4. 3D printing

For this study, the 3D printed compression sensors were fabricated into cubes. The constant cross section of this shape, vertically and laterally, allow for easy measurement of electric resistivity and conductivity. A 3D model of a cube (8x8x8 mm) was created using the software Solidworks, saved as a stereolithography (STL) file, and sliced into G-code using Slic3r. The PDMS/CNT ink was mixed with the PDMS part B catalyst (using the manufacturer suggested 10:1 prepolymer to part B ratio) and loaded into a 3mL syringe capped with a needle of varying sizes. After loading the syringe into the 3D printer, the material was printed at the desired print speed on an aluminum plate and cured in an oven at 150 ºC for 1 hour. Figure 6 shows a schematic illustration of the sensor fabrication. Figure 7 shows the layer by layer printing of the nanocomposite compression sensors into a truncated cone as an example geometry.

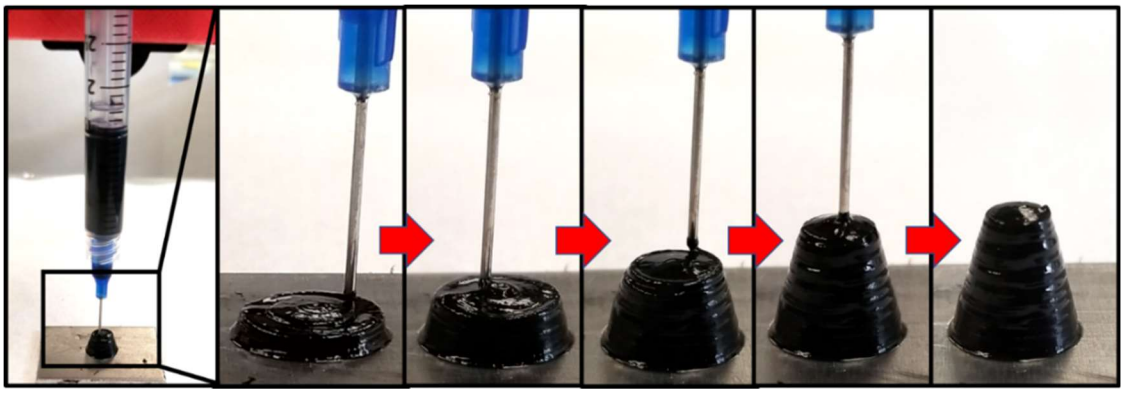

Figure 7. Layer by layer 3D printing of free standing PDMS/CNT [49].

3D printing is highly versatile and customizable process which allows the user to control manufacturing parameters such as print speed, layer height, and print direction or pattern. In this work, 3D printed samples were fabricated with two different print patterns, concentric and rectilinear. The sliced models are shown in Figure 8, where Figure 8a is the concentric printing pattern and Figure 8b is rectilinear. Interlayer adhesion was studied visually by dissection of a 3D printed cube from each 3D printing pattern to search for any inconsistencies and layer delamination.

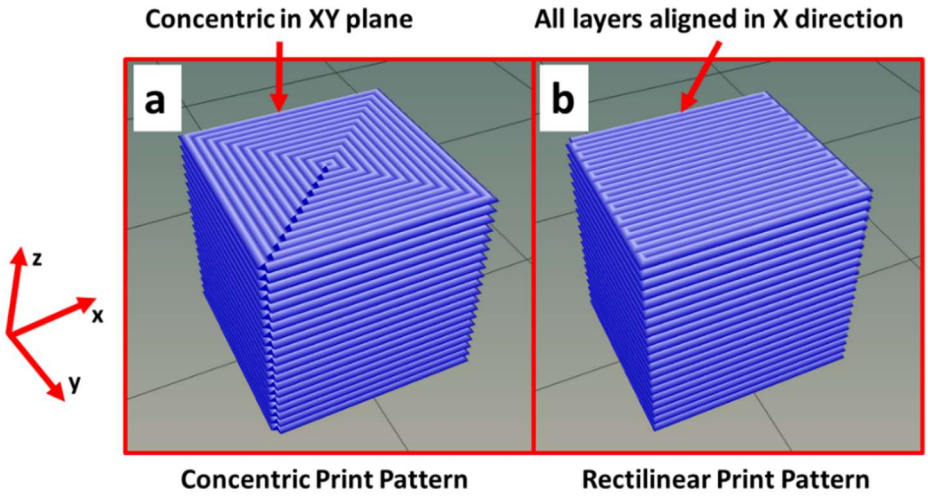

Figure 8. Sliced 3D printed patterns - (a) concentric and (b) rectilinear.

2.2.5. Cast Sample Fabrication

To fabricate the cast samples, the PDMS/CNT ink was measured out into a plastic weighing boat and mixed with the catalyst at the manufacturer recommended 10:1 prepolymer to catalyst ratio. The ink was then scooped into an aluminum cast to create 8x8x8 mm PDMS/CNT nanocomposite samples. The mold used for this purpose is shown in Figure 9.

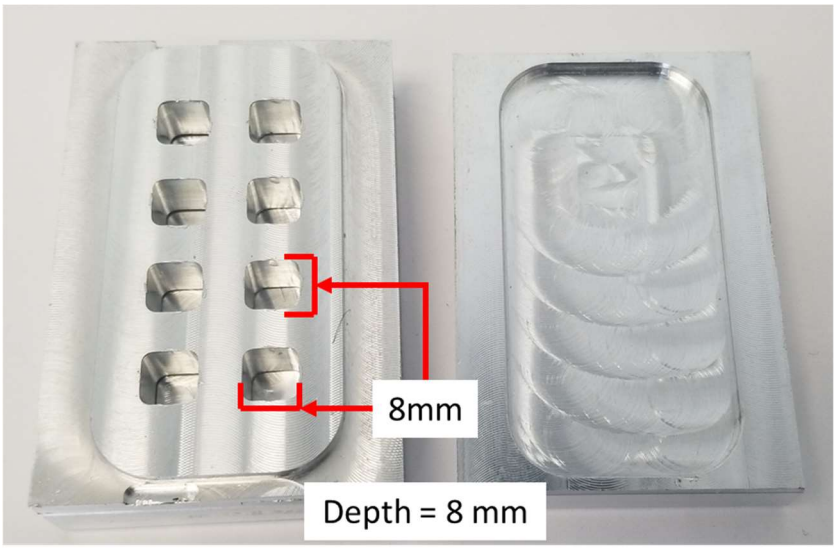

Figure 9. Mold used to create cast samples.

2.2.6. Porosity measurements

To quantify the porosity within the 3D printed samples, the sensors were subjected to a density test using the water cup technique. This simple technique compares the weight of a cup of a known volume with water before and after a sample is dropped into it. The density of the sample can be extrapolated from equation (6),

$$W = W_c + W_w - W_s + \rho_w V_s \qquad (6)$$

where W is the weight of the whole system, W_c is the weight of the cup, W_w is the weight of all water that can fit in the cup, W_s is the weight of the sample, ρ_w is the density of water, and V_s is

the volume of the sample. By measuring the volume of the sample, the density can be calculated from the known weight. The densities of the cast samples were measured and assumed to be 100% and was used as a comparison point for the 3D printed samples. The porosity is calculated per equation (7),

$$Porosity = 1 - \frac{\rho_{printed}}{\rho_{cast}} \qquad (7)$$

where ρ_{cast} and $\rho_{printed}$ are the densities of the cast and printed samples, respectively.

In addition, to understand the morphology of the pores and their distribution, scanning electron microscope (SEM) images were taken using a Zeiss Neon 40esb SEM. Images were taken of the sample with the best and worst porosity for comparison.

2.2.7. Resistivity/Conductivity Measurements

Resistivity measurements were carried out on PDMS/CNT nanocomposites of CNT concentrations between 1.5% and 3.0%, for 3D printed samples, and between 1.0% and 3.0% for cast samples. Electrodes in the form of copper tape were attached to the samples using silver epoxy. Silver epoxy is a two part highly conductive adhesive (resistivity of 0.007 Ω-m) with a working time of about 10 min and a full cure time of 15 min at 65 ºC or 24 hrs at room temperature. For this experiment, the silver epoxy part A and part B were mixed in equal parts and spread to cover opposing surfaces of a sample. Two 1 x 0.5 inch pieces of copper tape was applied on the adhesive. This was repeated for all samples, and they were left to cure for 24 hrs at room temperature. To collect resistivity data, each of the leads (copper tape) were connected to an Agilent 34401a multimeter, and the resistance was recorded for 60 – 70 seconds. Equations (3) and (4) were used to calculate resistivity (ρ) and conductivity (σ).

2.3. Results

2.3.1. Rheology

To explore the nanocomposite ink's yield point at varying CNT content, oscillatory rheology tests at a frequency of 1 Hz were performed for PDMS/CNT nanocomposites with 1.0 – 3.0 wt% CNT content. In the case of 3D printed thermosetting nanocomposites, the yield point of the material must be such that the material does not deform under its own weight once 3D printed into the final geometry. In this experiment, the samples printed are relatively small and do not weigh much (around a 0.5 g). Thus, this study is performed to verify whether a yield point is present and proceed with the experiment using those inks that possess one.

The results of the oscillatory shar test are shown in Figure 10 (*G'* and *G''* are the storage and loss modulus of the material, respectively). The storage and loss modulus can be considered as the solid and viscous properties of a material, respectively. From these values, there are two main ways by which the yield point can be assessed: the location where the *G'* begins to decrease before falling to a value below *G''*, and the crossover location of *G'* and *G''*. For this work, the latter of the two methods is used. The resulting yield point values are tabulated in Table 1, and the yield point location for each set of curves is shown in Figure 10 in the form of a circle at the modulus crossover.

At CNT contents of 0.0 (pristine PDMS) and 1.0 wt%, the inks display no yield point. However, as the CNT content reaches and passes 1.5 wt% the nanoparticles behave like a thixotropic agent by endowing the nanocomposite ink with a yield point. Moreover, as the CNT content increases, so does the storage modulus (G'), indicating higher elastic properties from inks with a higher CNT content. Having studied the rheology of all inks, those with a yield point will be used for 3D printing, and those without will only be used in casting.

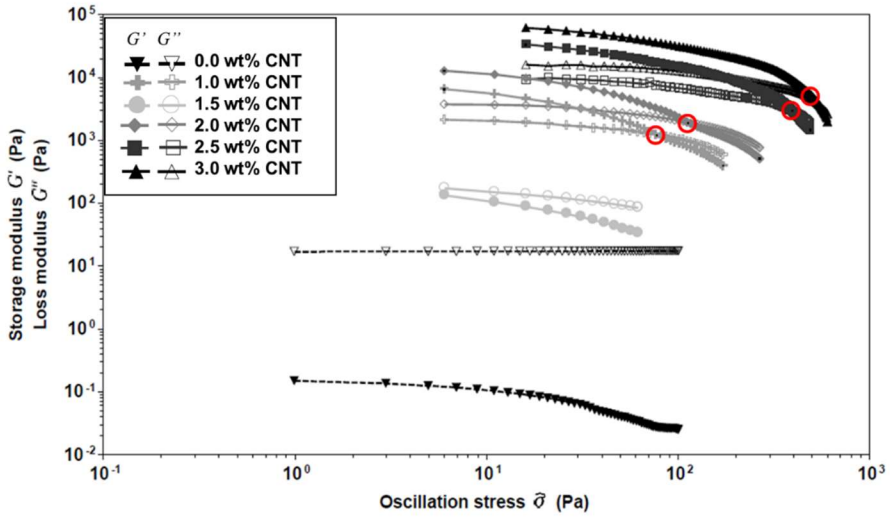

Figure 10. Amplitude sweep rheology test results for PDMS/CNT inks with 1.0 to 3.0 wt% CNT content.

Table 1. Yield point values extracted from the rheological oscillatory test.

CNT Content (wt%)	Yield Point (Pa)
0.0	N/A
1.0	N/A
1.5	77.33
2.0	113.21
2.5	393.52
3.0	547.26

2.3.2. 3D Printing

Trimetric views of the rectilinear and concentric 3D printed cubes are shown in Figure 11a and Figure 11b, respectively. The axis in the center column of the figure helps to orient the final 3D printed nanocomposite with respect to the sliced computer-generated version in Figure 8. In addition, an X-Z in-plane view of the rectilinear and concentric 3D printed cubes is shown in Figure 12a and Figure 12b, respectively. The surface morphology shows a high dependency on the 3D printing pattern, with the rectilinear 3D print showing a tendency to become slightly compressed along the X axis.

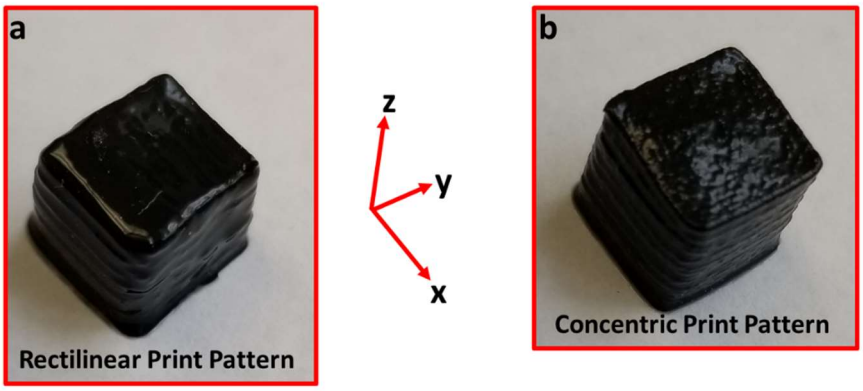

Figure 11. Trimetric views of the resulting 3D printed cubes from (a) rectilinear and (b) concentric patterns.

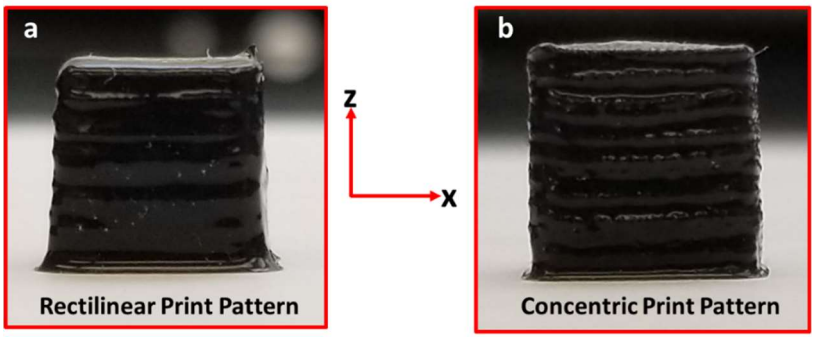

Figure 12. X-Z in-plane view of the (a) rectilinear and (b) concentric 3D printed cubes.

To explore the interlayer adhesion of the 3D printed nanocomposites, a resulting sample from each 3D printing pattern was dissected (Figure 11e and f). Each sample was cut laterally along the X direction. Neither print pattern shows signs of weak interlayer adhesion. In fact, both samples show full bonding between each layer, similar to what would be found in a cast sample. The horizontal features shown are a result of the cutting process, which leaves undesired topography in the polymer as a result of the razor gliding across the material. This interlayer bonding is ideal for nanocomposite sensors as it allows the CNTs to penetrate across layers.

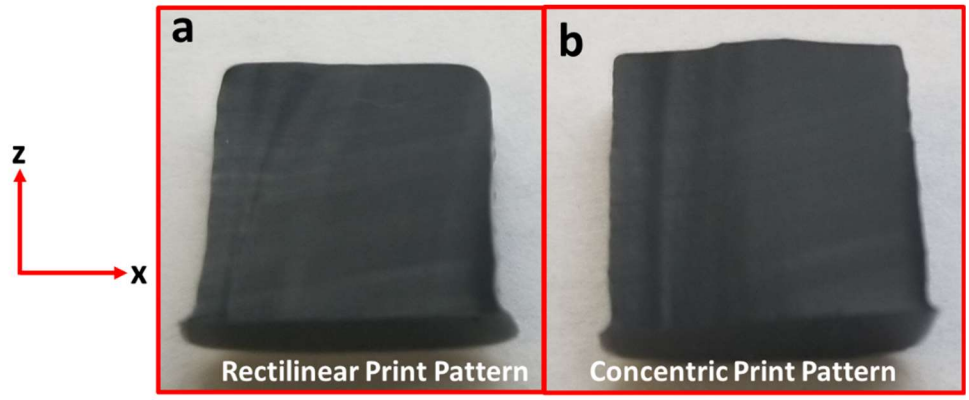

Figure 13. Cross section of 3D printed samples using the (a) rectilinear and (b) concentric printing patterns.

2.3.3. Porosity

One factor that may influence the consistency of the final mechanical and electrical properties of the 3D printed sensors is the presence of porosity. Pores are commonly observed in 3D printed thermoplastics due to gaps between filamentary depositions in the printing pattern. In addition, adhesion between layers may be affected by previous layer cooling or temperature gradients within the print. In the case of functional inks, the main cause of pores during printing is the rheology of the synthesized material.

To quantify the porosity in 3D printed samples of PDMS/CNT nanocomposites with CNT contents of 1.5 to 3.0 wt%, the density cup technique was employed. Porosity results for rectilinear and concentric prints are shown in Figure 14. Although both rectilinear and concentric printed samples displayed similar porosity results, rectilinear prints showed a slightly lower porosity when printing concentrations ranging from 1.5 to 2.5 wt% CNT. Porosity increased with CNT content, up to about 9% for concentrations of 3.0 wt% CNT. The low porosity in the samples with lower CNT loading can be attributed to voids within the ink filamentary extrusions. However, the larger porosity of the higher loading samples may be a process induced phenomenon as a result of rheological effects due to increased CNT loading.

To further explore the morphology of the pores, samples from the best case (i.e. lowest porosity; 1.5 wt% CNT) and worst case (3.0 wt% CNT) scenarios for both 3D printing patterns were imaged under SEM to compare their pore morphology. Images of the cross section of samples printed with 3.0 wt% CNT using rectilinear and concentric printing patters are shown in Figure 15a and Figure 15b, respectively. Similarly, cross sectional SEM images of the samples printed with the 1.5 wt% CNT ink in the rectilinear and concentric printing patterns are shown in Figure 16 and Figure 17, respectively. In these figures, the white arrows point to the pores, and the dotted arrows point out the printing direction. It should be noted that to collect cross-sectional images, samples were cut in the direction of printing for rectilinear printed samples, and in the XZ plane for concentric printed samples. The cutting direction can be identified in the figures by the parallel horizontal streaks in the polymer, which can be clearly seen in the low magnification images.

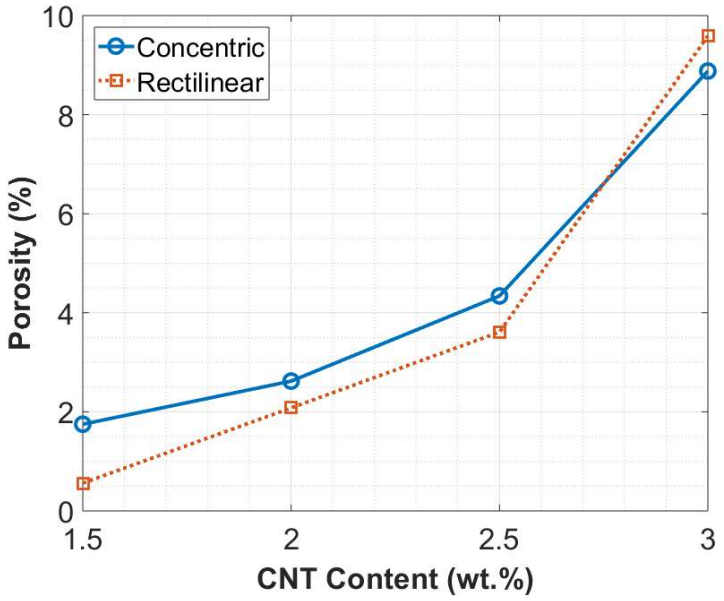

Figure 14. Porosity of 3D printed parts using the rectilinear and concentric printing patterns for PDMS/CNT nanocomposites with 1.5 to 3.0 wt% CNT loading.

Independent of printing pattern, printing with the 3.0 wt.% ink generates large pores on the order of hundreds of microns to millimeters. In this case, the pores are likely formed as a result of the filamentary extrusion dragging along the printed surface, rather than shearing off onto the print surface and depositing. This is less likely to happen in the first layer of printing, as the shear forces applied by the rigid print surfaces will be much higher than those of the polymer surface in the subsequent layers. The filamentary dragging phenomenon is more likely to occur as the CNT loading increases within the material due to the influence of the filler on the rheological properties of the polymer, most particularly the influence on G' [45]. A lower G' allows the material to relax and better bond with adjacent layers upon deposition, where the higher G' materials will tend to maintain their shape immediately after deposition. Moreover, if the storage modulus is too high, the shear forces generated by the previously deposited ink may not be enough to overcome the strength of the deposited material to remain as a single strand, thereby dragging along the printing

surface. This creates a gap in the printed layer that induces similar gaps in subsequently printed layers, as there is no surface to induce shearing of deposited polymer. This scenario is depicted in Figure 18. In addition, this rheological behavior may induce pore formation through a similar filament dragging mechanism when the print head makes sudden turns (i.e. 90^{o} turns for squares). In this scenario, the filamentary extrusion is not fully set in its location, thus when the printhead turns without slowing down or stopping, the extruded material is dragged along in a direction perpendicular to its appropriate deposition location, creating gaps between concentric squares. Both described phenomena are visualized during the printing process in Figure 19, where the voids are highlighted by the circles and ellipses in each image. Figure 19a demonstrates the voids occurring due to rapid turning, while Figure 19b and c demonstrate filamentary dragging creating millimeter scale linear voids.

In contrast, 3D printed specimen fabricated using the 1.5 wt% CNT ink displayed much smaller voids, on the order of single digit microns. Low magnification cross sectional SEM images of the rectilinear and concentric printed samples are shown in Figure 16a and Figure 17c, respectively. The porosity measurement study informed that higher pore content was expected out of samples fabricated using the concentric 3D printed pattern. Although finding these pores proved to be difficult even under SEM, areas imaged revealed more pores in the concentric printed sample. Due to their small size, these pores may be caused by several reasons. Although the previously discussed phenomenon of filamentary polymer dragging was more obvious for printing inks with 3.0 wt% CNT, it is difficult to conclude that this phenomenon is present when printing 1.5 wt% CNT ink. Notably, the diameter of the pores (~2-4 μm for those imaged) are significantly smaller than the diameter of the nozzle needle (410 μm), suggesting that it is possible that these voids may have been present in ink prior to printing. Pores of this nature could be formed as a result of THF

evaporation during material synthesis. As the THF content decreases while evaporating, the material begins to gain a yield point, such that further evaporation of THF will leave small voids that do not collapse. If this is the case, these pores may be reduced by centrifugation or planetary mixing of the polymer-loaded syringe before printing.

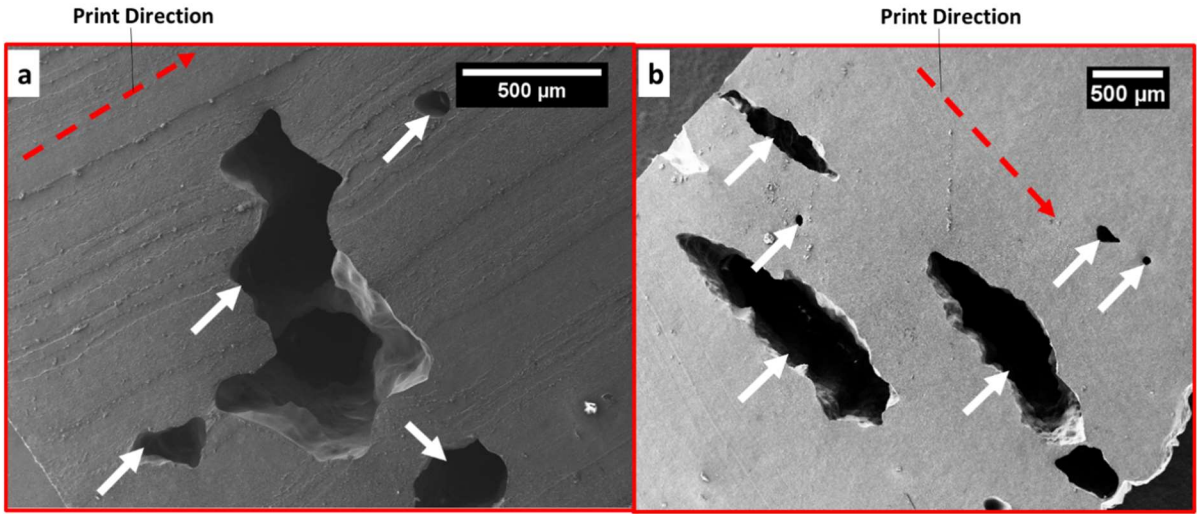

Figure 15. Low magnification (low mag) SEM Images of pores within 3D printed 3.0 wt% CNT content nanocomposites manufactured with the (a) rectiliinear and (b) concentric printing patterns. The dashed arrows in each image represent the printing direction, coincident with the bissection direction.

For this work, porosity experiments revealed that, although PDMS/CNT inks with 1.5 wt% CNT or higher possessed a yield point, not all inks would produce geometries with controllable infill ratios and internal macro-morphologies. From this study, we can conclude that reduced CNT content correlates with reduced porosity after 3D printing. Thus, the PDMS/CNT ink that produced the lowest porosity prints (1.5 wt% CNT) is ideal to print a solid structure However, with the goal of 3D printing piezoresistive sensors, it is imperative that the electrical properties of the material are studied prior to making this conclusion.

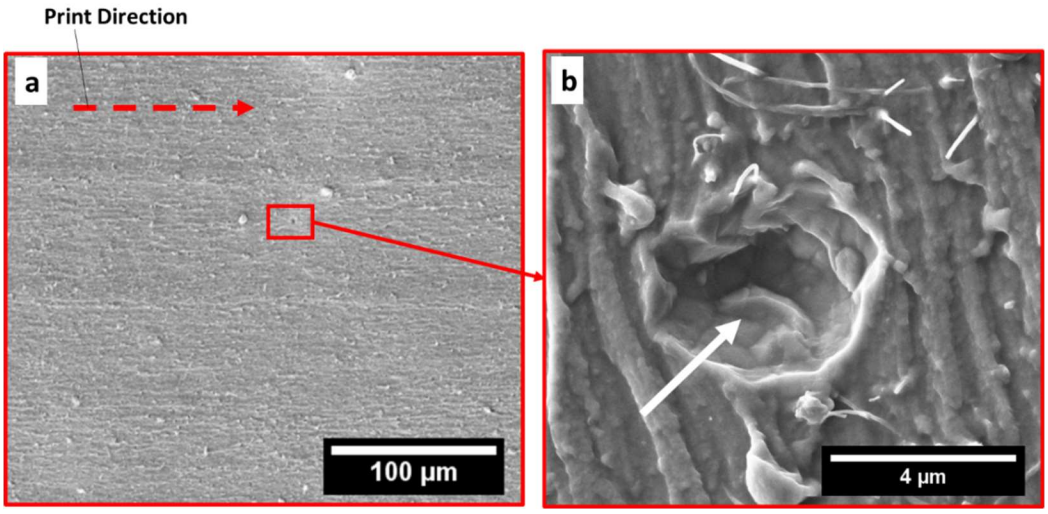

Figure 16. (a) low and (b) high mag SEM images of 3D printed 1.5 wt% CNT content nanocomposites manufactured with the rectilinear 3D printing pattern.

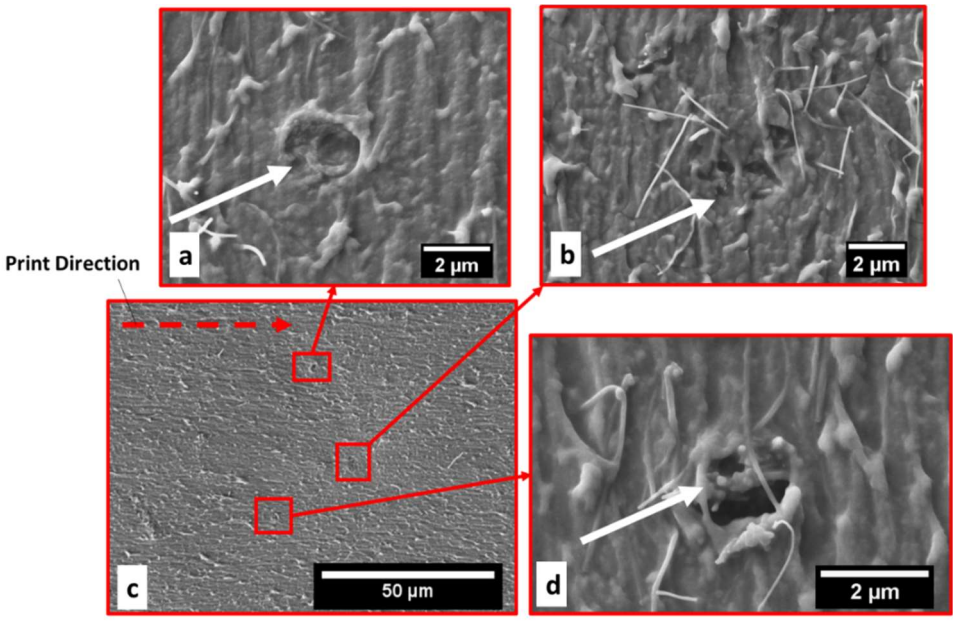

Figure 17. (a, b, d) High and (c) low mag SEM images of 3D printed 1.5 wt% CNT content nanocomposites manufactured with the concentric 3D printing pattern.

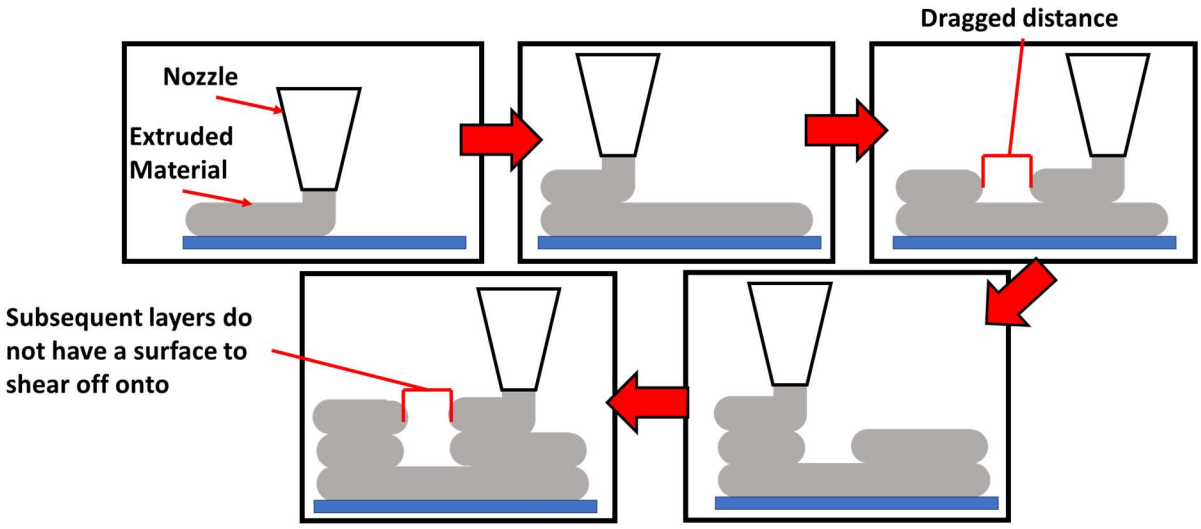

Figure 18. Layer by layer 3D printing process – filamentary extrusion is dragged across printing surface rather than deposited.

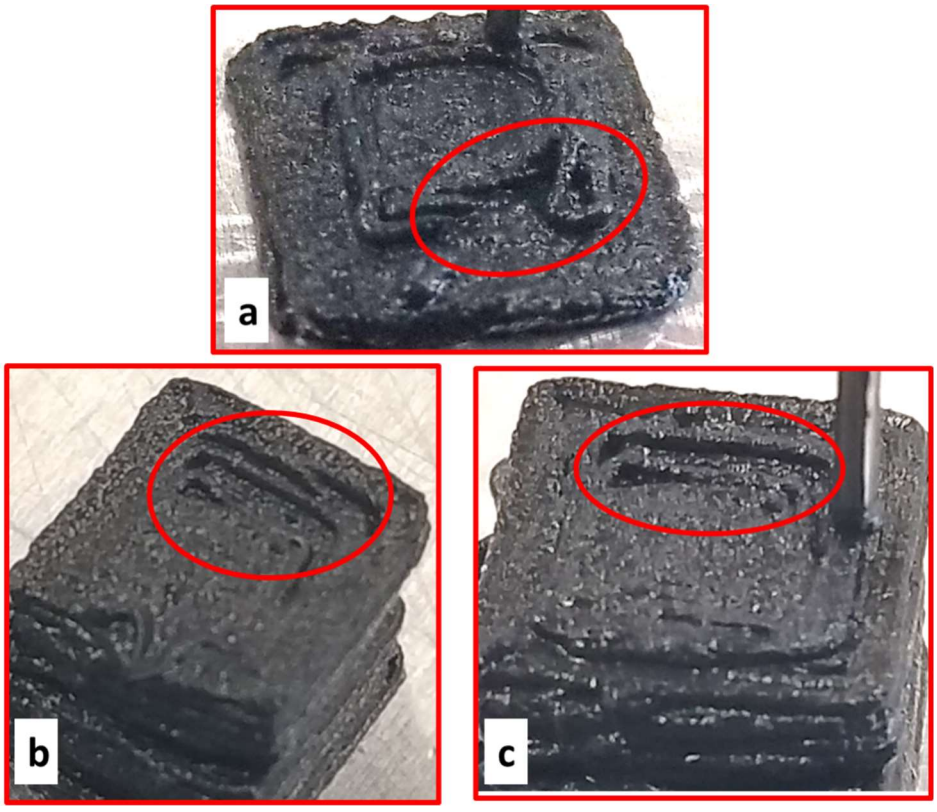

Figure 19. Examples of voids created while 3D printing with the 3.0 wt% CNT PDMS/CNT nanocomposite ink.

2.3.4. Resistivity/Conductivity Measurements

To assess which PDMS/CNT ink would yield the highest piezoresistive sensitivity, the resistivity and conductivity of inks with various concentrations of CNT were collected. Conductivity and resistivity were collected for cast samples containing 1.0-3.0 wt% CNT and 3D printed sample contained 1.5-3.0 wt% CNT. The 1.0 wt% ink was not printed because it did not possess a yield strength. However, it's cast conductivity and resistivity were measured to display the percolation trend of the material.

The resistivity and conductivity curves are shown in Figure 20a and Figure 20b, respectively. All three resistivity and conductivity curves (cast, rectilinear, and concentric) follow the same percolation pattern. However, the concentric 3D printing does show slightly higher resistivity and lower conductivity for most CNT wt% inks. In addition, the small size of the error bars for each data point on both graphs is evidence of the consistency from sample to sample within the same ink, regardless of fabrication method.

When creating a nanocomposite ink for piezoresistive applications, typically, the material with the highest resistivity (lowest conductivity) will yield the best performance. In compressive strain applications, this is because high resistivity signifies unfulfilled electric networks within the material, which can be completed by applying some pressure. The number of unfulfilled networks is higher for a material with lower concentration because the nanofillers will be more evenly spaced out. Additionally, lower nanofiller content make it easier to disperse the nanofillers within the matrix, as the maximum average theoretical distance at full dispersion is higher and can prevent re-agglomeration after cavitation under sonication. Ultimately, based on the electrical conductivity/resistivity and rheological characteristics of the material, it is concluded that the material concentration with the highest sensitivity potential is the PDMS/CNT ink with 1.5 wt%

CNT. Thus, for the remainder of this work, experiments performed to explore the 3D printing process effects on this material will involve only the 1.5 wt% CNT ink.

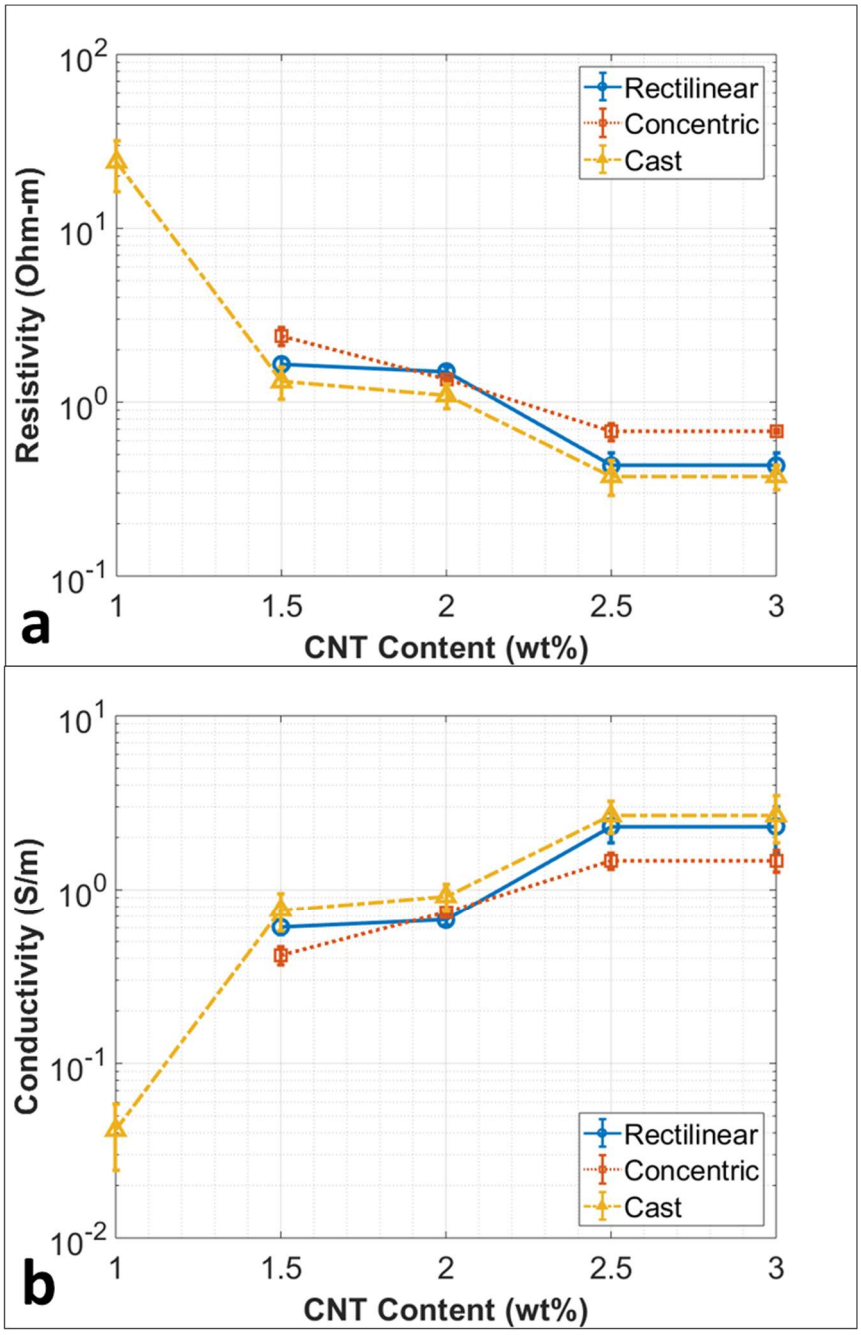

Figure 20. Resistivity and Conductivity for 3D printed and cast samples of different wt% CNT concentrations.

2.4. Conclusion

In this chapter, the CNT wt% of the PDMS/CNT nanocomposite ink was optimized for printability and piezoresistive sensitivity. The layer to layer lateral and vertical adhesion was visually investigated by cutting 3D printed samples laterally in the X direction to view their cross section. This revealed full adhesion between adjacent layers, similar to what would be expected from cast material. Furthermore, rheology experiments revealed the inks containing more than 1.5 wt% CNT possessed a yield strength, and thus, will maintain their fidelity while 3D printing after deposition from the nozzle. A porosity study exploring the density of the final 3D printed samples revealed that porosity increased with increasing CNT content in the PDMS/CNT ink. Finally, resistivity and conductivity data showed that the resistivity and conductivity decreased and increased, respectively, with the addition of nanofillers to the matrix, as expected. Additionally, this test revealed that when cast, the percolation curve of the PDMS/CNT nanocomposite follows the same pattern as its 3D printed counterpart, signaling little to no influence of the 3D printing process on the static intrinsic electrical properties of the material. From this chapter, it can be concluded that the optimal CNT content for the PDMS/CNT nanocomposite is 1.5 wt% CNT. This ink best combines 3D printability with highest piezoresistive sensitivity, aiding in the ultimate goal of manufacturing compression sensors.

CHAPTER 3. OPTIMIZATION OF 3D PRINTING PARAMETERS

3.1. Introduction

This chapter compares the piezoresistive performance of the 3D printed nanocomposite material to its cast counterpart. The main purpose is to explore the feasibility to replacing casted sensors with their 3D printed counterpart to improve customization, reducing the amount of waste material (via molds), and simplifying the fabrication process. In this regard, if 3D printed sensors can yield similar, or better, results as their cast counterpart, this hypothesis would be validated. The challenge with this experiment is that many processing parameters can influence the final performance of the sensors. This chapter addresses research objective ii, per section 1.4 of CHAPTER 1.

3.2. Experimental

3.2.1. Cyclic Piezoresistive Testing

To explore the piezoresistive performance of the 3D printed nanocomposite sensors, the sample's response to mechanical stimulus must be investigated. Each sample was placed between two copper plates mounted on plate fixtures on an Instron Single Column Universal Testing machine. The testing setup is shown in Figure 21. A cyclic displacement-controlled test was performed to compress each sample at 10% strain while collecting resistance data using an Agilent 34401a multimeter.

This cyclic test serves a multifaceted purpose, as it will allow for the exploration and optimization of 3D printing parameters. The rectilinear and concentric 3D printed shapes are tested to explore their isotropy. Each sample is tested under cyclic loading at 10% compressive strain at a crosshead speed of 1mm/min for 5 cycles, in all 3 axes. In addition, the effect of two different 3D printing parameters will be explored, print speed and needle size. Samples were printed using

printhead speeds of 1, 2, 4, and 8 mm/s and tested cyclically in the Z axis. Samples were also printed using needles sizes of 410, 710, and 1400 µm to explore the effect of nozzle size on the piezoresistive capabilities of the PDMS/CNT nanocomposite. For all tests, the collected resistance data was converted to relative resistance change and compared. Table 2 summarizes all samples 3D printed for this study that were studied under cyclic loading.

Table 2. Samples printed and tested (piezoresistivity).

Dimensions (mm)	**Print Pattern**	**Printhead Speed (mm/s)**	**Quantity**	**Needle Size (µm)**
8 x 8 x 8	Concentric	1	3	410
8 x 8 x 8	Rectilinear	1	3	410
8 x 8 x 8	Concentric	2	3	410
8 x 8 x 8	Concentric	4	3	410
8 x 8 x 8	Concentric	8	3	410
8 x8 x 8	Concentric	1	3	710
8 x8 x 8	Concentric	1	3	1400

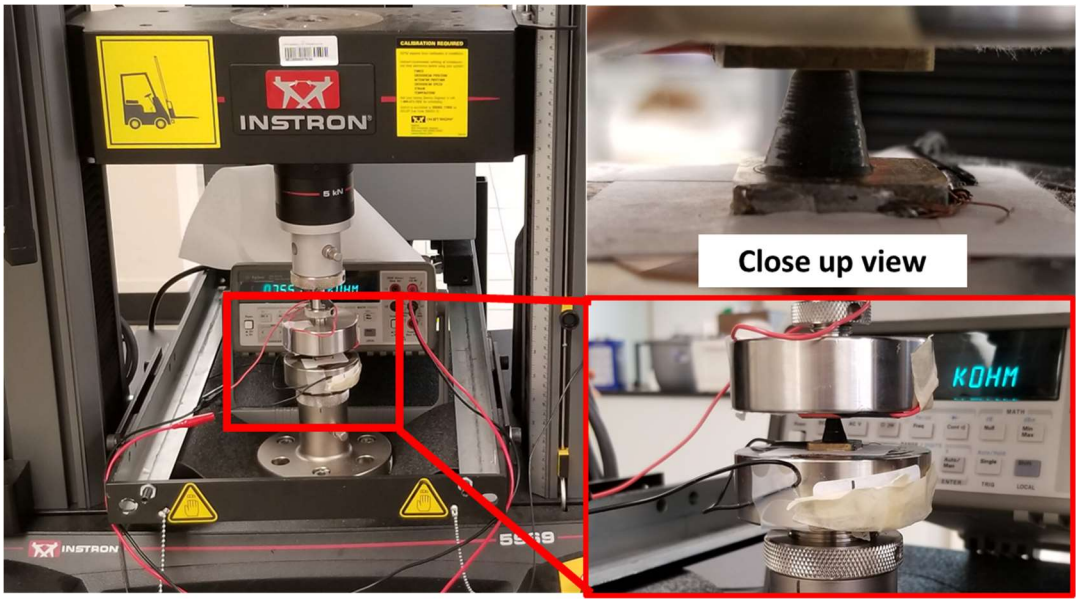

Figure 21. Test setup for cyclic piezoresistive testing [49].

3.3. Results

3.3.1. Isotropy Test

Cast sensors display isotropic behavior because the material is not added to the mold in any preferential method. However, researchers exploring 3D printed nanocomposites with various nanofillers have shown that additive manufacturing can cause process induced nanofiller alignment due to shearing of the extruded material [50-53]. In some cases, this alignment can induce a modest increase in certain material properties, such as mechanical and electrical, in the direction of the alignment.

Although beneficial in many applications, nanoparticle alignment may not be desired in additive manufacturing of some sensors. When 3D printing sensors of complex shapes, for example, the manufacturer may not desire preferential properties in various directions throughout the material. In addition, it is sometimes beneficial to print tall structures on their side to prevent the geometry from buckling or collapsing under its own weight and prevent other 3D printing

issues. Still, additive manufacturing remains more versatile than casting methods as the fabricated geometry can be easily edited using a CAD and slicer software package. Therefore, it is important to study the effects of 3D printing on the alignment of the nanofillers within the PDMS/CNT nanocomposite.

nanocomposite.

To test the isotropic behavior of the 3D printed sensors (both concentric and rectilinear printed), the piezoresistive response of the fabricated cubes was tested under cyclic loading at 10% strain and crosshead speed of 1mm/min in the X, Y, and Z axes. The results of the cyclic test are shown in Figure 22a and Figure 22b for the concentric and rectilinear 3D printing patterns, respectively Cubes printed with the concentric printing pattern showed ΔR/R values of 80%, 82%, and 85% for the X, Y, and Z directions, respectively. Similarly, the rectilinear printing pattern yielded a cube that output ΔR/R values of 83%, 81%, and 83% for the X, Y, and Z directions, respectively. The relative resistance change values in all 3 axes are relatively close for both 3D printed shapes, thus, both shapes can be considered isotropic. In addition, all 3 axes showed highly repetitive behavior, signaling a lack of electronic network breakdown in all samples tested. Likewise, mechanical response data gathered from these tests reveal little difference between the compressive Young's modulus of the X, Y, and Z axis of the printed cube. In fact, all values are within the error bars within the same printing pattern, revealing that the 3D printing process does not produce anisotropic performance in the mechanical behavior of 3D printed specimen. A bar graph comparing the compressive Young's modulus values of the 3D printed shapes in all axes and a table detailing these values are shown in Figure 23 and Table 3, respectively.

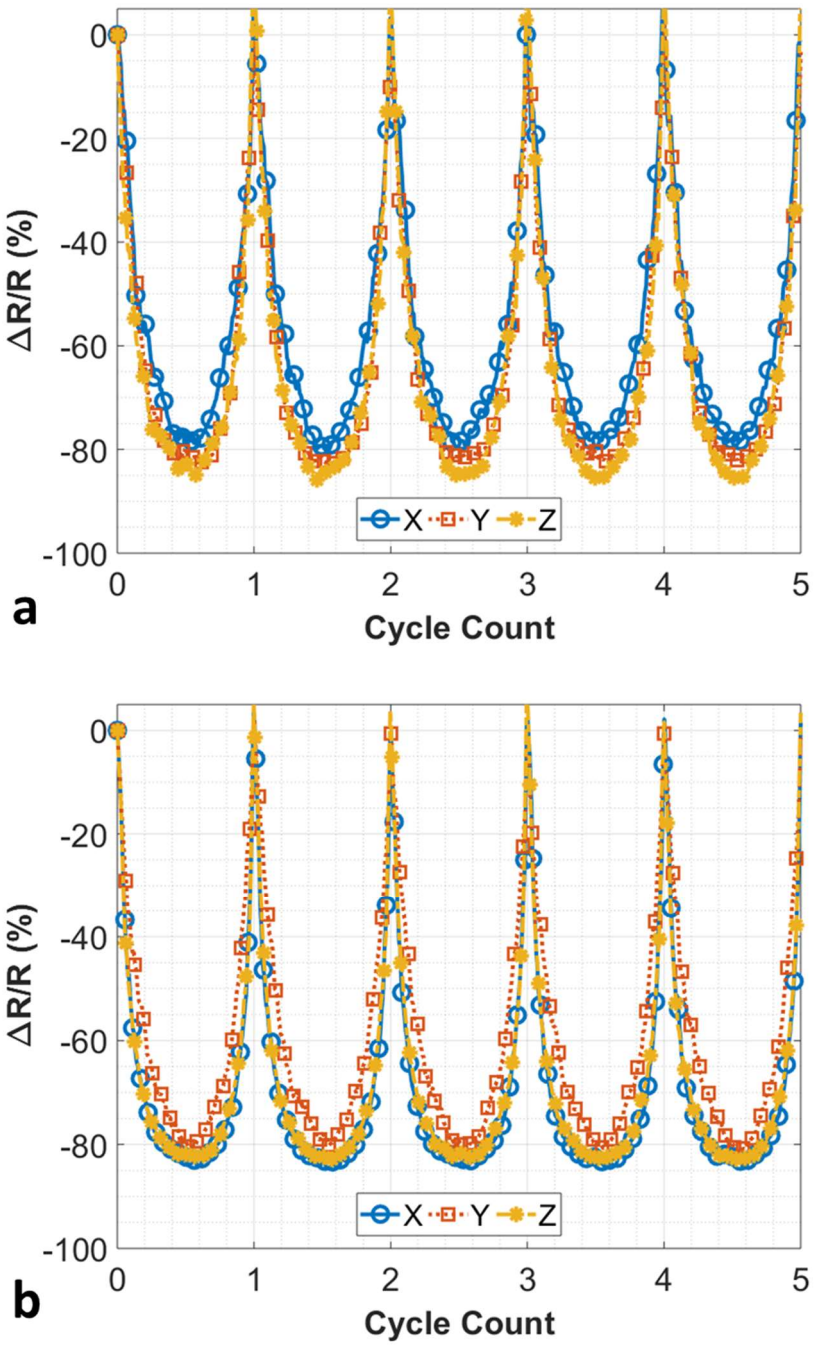

Figure 22. Isotropy study comparing the piezoresistive response of the printed PDMS/CNT nanocomposite in all 3 axes for the (a) concentric and (b) rectilinear 3D printing patterns.

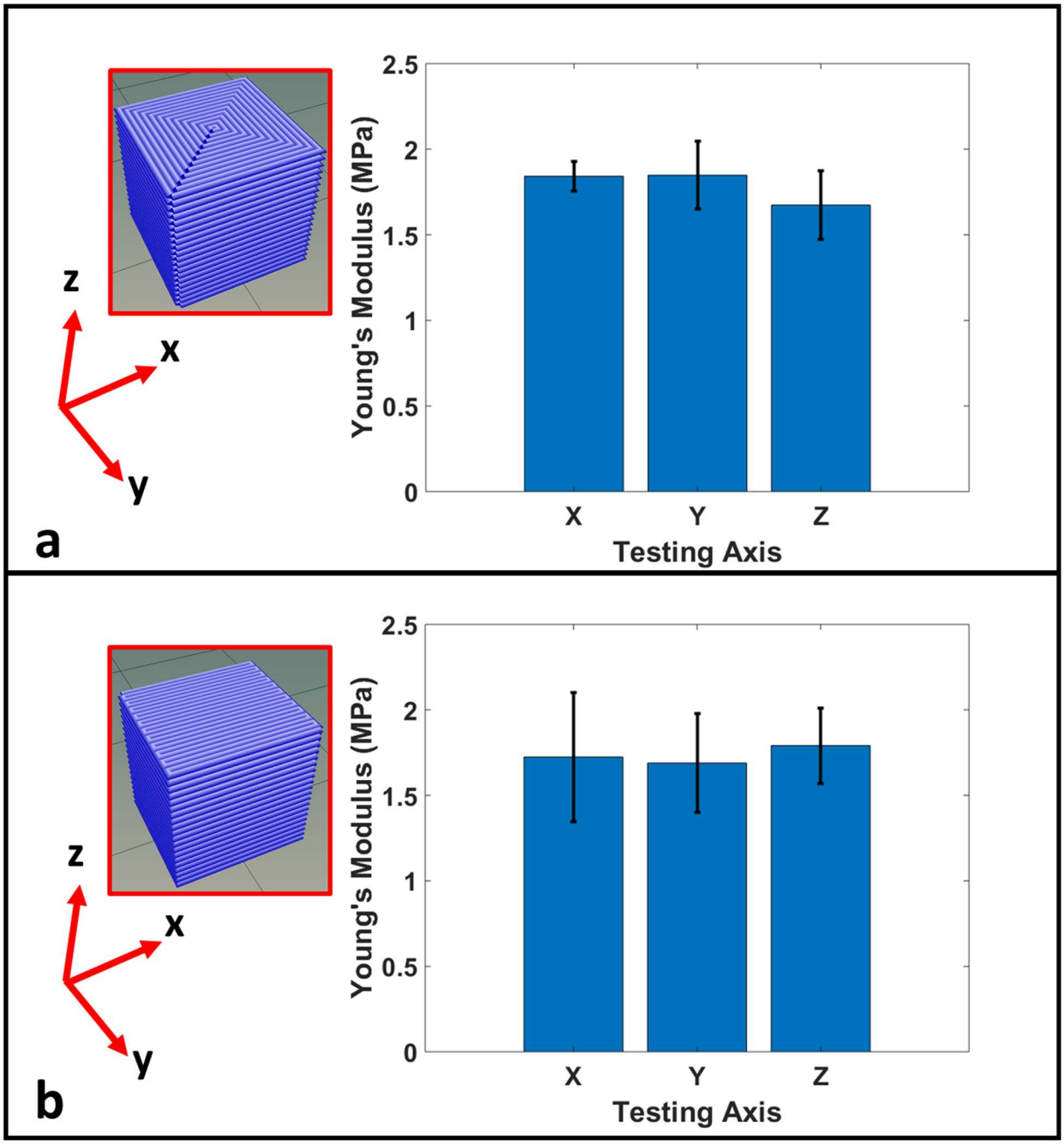

Figure 23. Compressive Young's Modulus in the X, Y, and Z axes for printed PDMS/CNT ink nanocomposite with 1.5 wt% CNT content – (a) concentric and (b) rectilinear 3D printing patterns.

Table 3. Young's Modulus values in the X, Y, and Z axes for printed PDMS/CNT nanocomposite.

Printing Pattern (Axis)	Compressive Young's Modulus (MPa)
Concentric (X)	1.84 ± 0.09
Concentric (Y)	1.85 ± 0.20
Concentric (Z)	1.67 ± 0.20
Rectilinear (X)	1.72 ± 0.38
Rectilinear (Y)	1.69 ± 0.29
Rectilinear (Z)	1.79 ± 0.22

3.3.2. Piezoresistive Behavior – 3D Printed vs Cast

Although both 3D printed sensors displayed isotropic behavior, their piezoresistive response must be compared to that of their cast counterparts to support understand whether they may be used to replace casting. As such, a cast sample of the same PDMS/CNT 1.5 wt% CNT ink was tested under cyclic loading at 10% strain using a 1mm/min crosshead speed. Resistance results were gathered throughout the test and compared to those of the 3D printed samples. It should be noted that because the 3D printed samples displayed isotropic behavior, the Z axis was chosen to compare the results to the cast material. The results of the five-cycle test comparing cast and 3D printed samples is shown in Figure 24. The average relative resistance change of 3D printed samples, concentric and rectilinear, and cast samples was very close, measuring at 85%, 82%, and

81%, respectively. Moreover, all three fabrication techniques produced samples with similar sensing characteristics in both the loading and unloading phase of the test. This is important because, although these sensors can be designed to undergo a specific compressive strain or pressure, mechanical stimulus may be a dynamic input.

In addition to showing no 3D printing dependence on the piezoresistive properties, the mechanical behavior of cast samples closely matched that of the 3D printed ones. A comparison of the compressive Young's modulus of cast and 3D printed samples (both printing patterns) is shown in Figure 25. Although there is slight variation between the thee values, it is important to note that all three fall within their error bars. Deviations in the mechanical behavior in this experiment are likely due to the slightly porous nature of the fabricated samples. This is corroborated by the fact that the mechanical response of the 3D printed samples printed with the rectilinear pattern (~0.5 % porosity) closely matches that of the cast, while the response of the concentric printed sample (~2.5% porosity) is slightly lower.

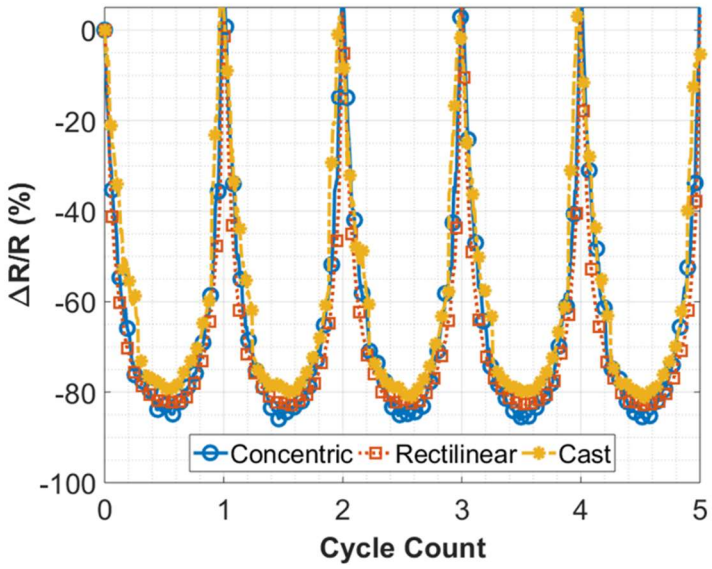

Figure 24. Piezoresistive response of cast, sensors compared to 3D printed counterparts.

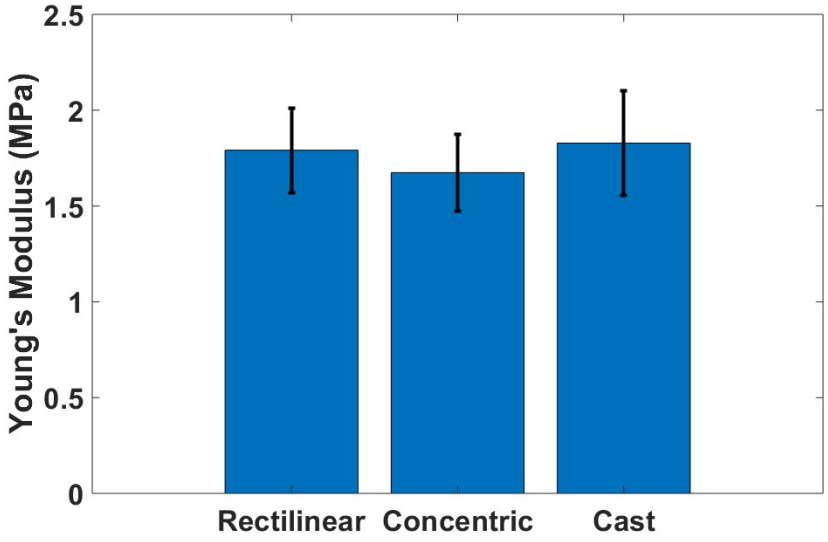

Figure 25. Mechanical response of cast, sensors compared to 3D printed counterparts.

Although these results prove that the 3D printed sensors are isotropic and a viable alternative to casted samples, the question remains as to why the expected nanofiller alignment is not influencing the results as discussed in previous works [50-53]. This is likely because the resulting nanocomposite, once cured, has no alignment.

To understand the initial alignment, we can visualize the flow out of a 3D printer nozzle (Figure 26a). With nanocomposite functional inks, such as the one in the present study, the material experiences high shear forces as it is extruded from the depositing nozzle. As the ink is extruded, intra-material interactions due to the converging nozzle and shear due to the narrow needle walls en-route to the extruder exit cause nanofillers (especially those with a high aspect ratio) to rotate as they are expelled normal to their shorter dimension (in the case of nanotubes, perpendicular to their diameter). Once deposited, the nozzle induced alignment remains, assuming the nanocomposite possess rheological properties which will prevent it from wetting the surface or flowing in such a manner to induce nanofiller motion and reorientation (Figure 26b) [54]. This is the case when printing thermoplastic materials, as they cool quickly after deposition, essentially

locking any nanofillers in their aligned orientation. When functional inks are printed, rheological properties must allow for quick polymer recovery to prevent flow after deposition, and a high enough yield point to overcome any internal forces which may influence reorientation [45]. In addition, the time between deposition of the polymer and material curing may also affect alignment [54]. The present study is not sufficient to characterize the importance of these variables, but it is important that they are mentioned to understand the interactions at play.

Perhaps the largest distinction between the aforementioned scenarios and the one in this study, however, lies in the 3D printing process. When 3D printing the solid cubes for this work, filamentary polymer lines were extruded directly adjacent and slightly overlapping those previously deposited to ensure proper lateral and vertical adhesion. When this additional material is deposited, previous alignment is reorganized due to the interaction between adjacent lines. This can be due to a disturbance of the original line by the nozzle passing as it is depositing new material and/or the interaction between the lines as they settle and merge during polymer recovery (Figure 26c). It should be noted that this phenomenon of alignment disturbance due to adjacent filamentary extrusions is limited to interacting sections of adjacent depositions. Except for ink deposited on the faces and edges of the cube, most material will experience interactions with at least four adjacent filamentary deposition (two on each side, above, and below). Thus, because each interaction causes a disturbance to a portion of each extrusion, the superposition of all four disturbances results in loss of most alignment within the filament. If there is a gap between two filamentary deposition, however, alignment would go undisturbed, and filler orientation would revert to the well understood scenario (Figure 26b). Moreover, due to the length of time to print the samples discussed thus far, nanofillers within the matrix which may have maintained alignment will rearrange due to interparticle interactions and diffusion [54]. In the present study, solid

structures are manufactured by using a 100% infill, rather than the more porous scaffolding used for conventional printing, leading to full adhesion between layers and isotropic properties dependent on the manufactured geometry.

It should be noted that since 3D printed geometries showed isotropic properties for both rectilinear and concentric printing patters, only one of the two will be chosen to further explore processing parameters in the remainder of this work. In this case, the concentric printing pattern was chosen to continue due to the higher geometric quality of the resulting prints. Because concentric printing continuously outlines the final desired shape, the resulting geometry offers a smoother surface finish leading to better contacts with electrodes for easier resistance data collection during compression tests, as surface morphology effects are minimized.

3.3.3. 3D Printing Parameters

To confirm the hypothesis explained in Figure 26 it is important to explore the effect of 3D printing parameters on the final printed parts. For this study, the two parameters selected were nozzle diameter and print speed as they both can affect the shear on the printed ink and, therefore, the state of alignment of the nanofillers due to varying nozzle pressures. Samples were printed at four printing speeds between 1 and 8 mm/s with a nozzle diameter of 410 µm. In theory, increased printing speed increases the shear forces applied on the deposited material in the printing nozzle due to increased nozzle pressure as more material is extruded, thereby inducing enhanced alignment as the printhead speed increases. Samples were tested under cyclic loading at 10% strain while resistance data was measured. A comparison of the piezoresistive behavior of samples printed at varying print speeds is shown in Figure 28a. The piezoresistive response was almost identical for the samples printed at all four speeds. This is likely due to the filamentary interaction alignment disturbance phenomenon previously described.

Table 4. Print times for samples printed at varying print speeds – concentric printing pattern.

Print Speed (mm/s)	Print Time (min:sec)
1	75:35
2	37:52
4	19:00
8	9:34

To further explore the effect of processing parameters on the piezoresistive response of 3D printed specimen, samples were printed with 3 nozzle diameters ranging from 410 to 1400 μm at a print speed of 1mm/s. Samples were cyclically tested at 10% strain with a crosshead speed of 1mm/min while recording resistance data. The 5 cycle piezoresistance results for the printing speed and nozzle diameter study are show in Figure 28b. Theoretically, because the nozzle diameter is increasing, the proportion of the interaction area (where adjacent filamentary depositions disturb each other's alignment) to the undisturbed area should decrease. This phenomenon can also be understood by considering that in fluid flow, as the distance from the wall increases, the fluid will experience less shear stress. Therefore, increasing the nozzle size will increase the shear gradient between the center of the needle and the walls. This could be exhibited physically by the samples via differing piezoresistive responses at varying printing needle sizes. However, the piezoresistive results for samples printed at varying nozzle sizes show that nozzle size does not affect the sensing performance. Although the shear in the depositing nozzle induces alignment of nanofillers, it is possible that this alignment is not uniformly distributed within wider nozzles, resulting in better

alignment in areas with higher shear (Figure 27a). In this case, the fillers adjacent to the nozzle walls would display higher alignment after deposition. Thus, when layers are deposited adjacent to each other, not only does the area of disturbance between the two filamentary extrusions suffer a loss of alignment, but a non-trivial portion of the deposition is already unaligned (Figure 27b). This may explain the similar piezoresistive response measured at all nozzle sizes. This theory is illustrated in the schematic shown in Figure 27.

Table 5. Print times for samples printed at varying nozzle sizes – concentric printing pattern.

Nozzle Size (μm)	Print Time (min:sec)
410	75:35
710	26:26
1400	11:10

In addition, a second alignment disturbance mechanism lies in the time required to print each individual sample. As the time to print increases, the diffusion alignment disturbance phenomenon also begins to take effect, whereby, as the polymer rests on the printing surface post deposition, filler within the polymer will begin to shift and rearrange due to filler-filler interactions [54]. The times to print the 8x8x8 mm sample used in this study with each printing speed and nozzle size are shown in Table 4 and Table 5, respectively.

Because the sensing response of this material is independent of 3D printing nozzle size and print speed, this method could be employed to print sensors of complex shapes with the option of

using a smaller nozzle size for geometrical accuracy or larger nozzle size for high output. A similar result was demonstrated by Christ et al. showing that a polyurethane/CNT nanocomposite displayed similar piezoresistive behavior in its filamentary form (prior to 3D printing) and after 3D printing [11].

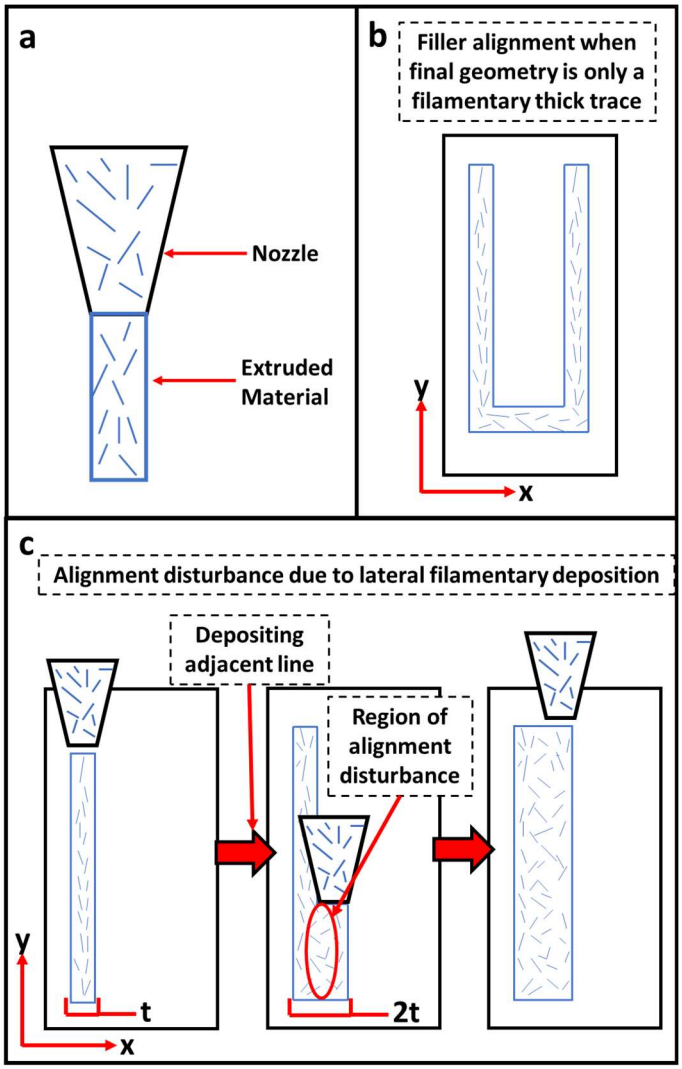

Figure 26. (a) Widely understood nozzle induced nanofiller alignment; (b) nanofiller alignment post-deposition; (c) nanofiller de-alignment due to interactions between adjacent layers.

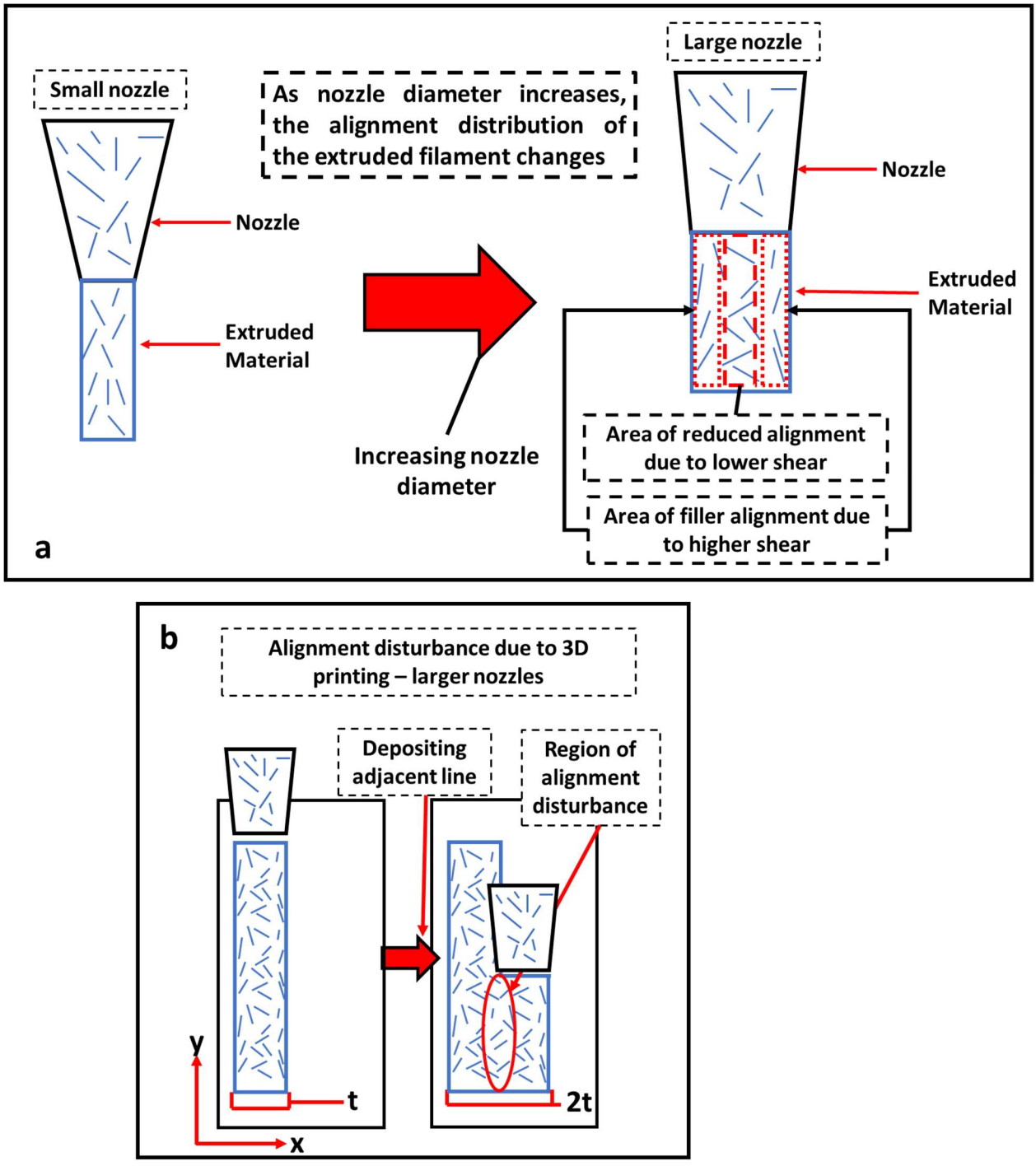

Figure 27. (a) Comparison of shear induced alignment in small and large nozzles; (b) CNT de-alignment due to interactions between adjacent layers (large nozzle).

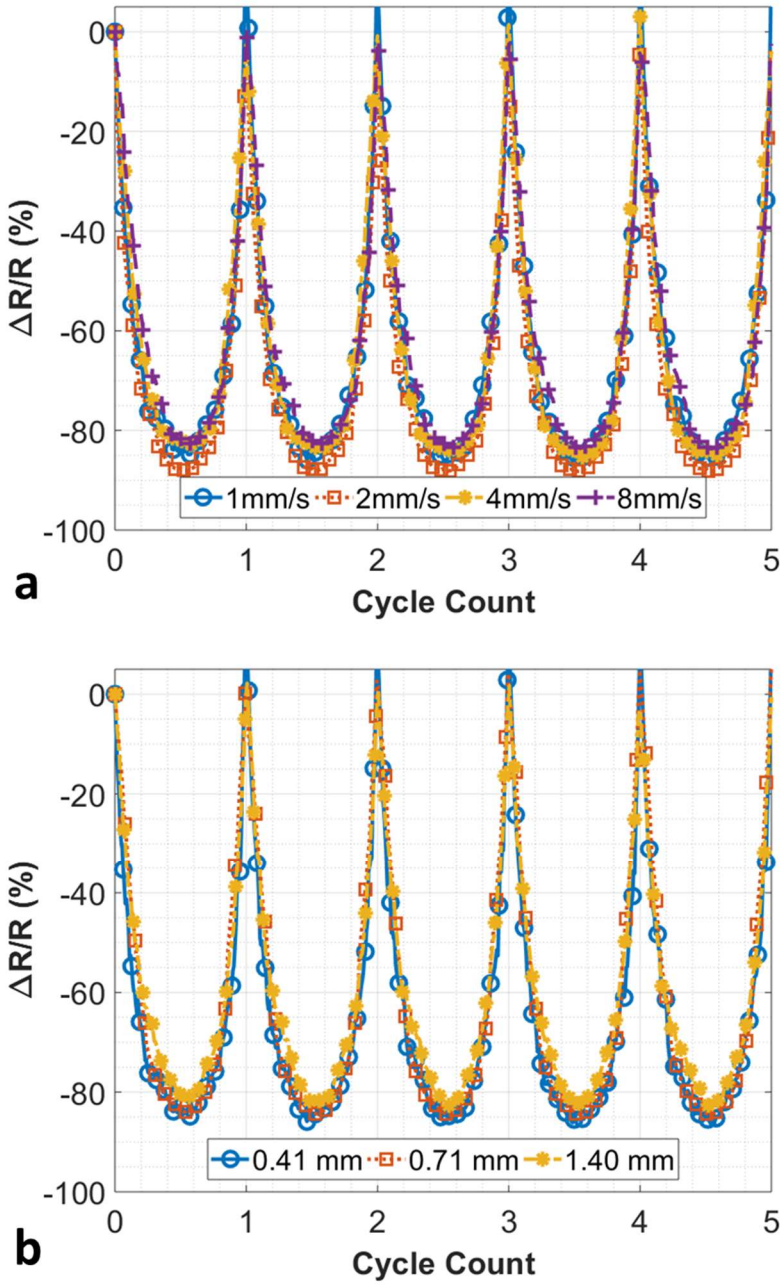

Figure 28. 3D printing parameter effect – cyclic piezoresistance test results for (a) variation for printing speed and (b) variation of nozzle size.

3.4. Conclusion

In this chapter, the effect of 3D printing and processing parameters on the piezoresistive response of the PDMS/CNT sensors was explored. The sensors, printed using a PDMS/CNT ink with 1.5 wt% CNT, were tested under cyclic compression, at 10% strain and a constant crosshead speed of 1mm/min, while collecting resistance data. Testing each axis of the cubic sensors independently revealed that for both rectilinear and concentric printed sensors, the piezoresistive response from all 3 axes matched closely. This signals that the 3D printing process did not induce any anisotropic properties in the final printed part. Although previous studies have shown nanofiller alignment due to 3D printing, we argue that this phenomenon does not apply to bulk 3D prints with thermosetting polymers due to interactions between vertical and lateral filamentary depositions. In addition, comparison between the piezoresistive response between samples fabricated with rectilinear and concentric printing patterns and cast reveal that all three match very closely. This reveals that the performance of 3D printed sensors is independent of printing pattern and unchanged to that of cast samples. This establishes 3D printing as an alternative fabrication method to casting. Further, to explore the effect of 3D printing parameters on the piezoresistive performance of the final nanocomposite sensors, the nozzle needle size and printing speed were changed. Samples were printed using a 410 μm nozzle needle, while varying the printing speed between 1 and 8 mm/s. Similarly, samples were printed at 1mm/s using nozzle needle sizes of 410, 710, and 1400 μm. All samples, regardless of printing speed or needle size, displayed very similar performance. This study sheds light on the viability of 3D printing sensors in lieu of casting. Moreover, because 3D printing parameters do not induce a change in electrical properties, this nanocomposite sensor fabrication process can be adapted to fit the needs of the user, whether that

is using a smaller nozzle and slower printing speed for geometry accuracy, or larger nozzle size and higher printing speed for faster output.

CHAPTER 4. PIEZORESISTIVE SENSOR CHARACTERIZATION

NOTE: Portions of this chapter have been published as a journal publication (see reference [49])

4.1. Introduction

To fully explore the piezoresistive response of the PDMS/CNT nanocomposite, a full characterization of a sample sensor is required. In this chapter, full piezoresistive and mechanical characterization is performed. The sensor's microstructure and morphology are studied via a scanning electron microscope (SEM). The sensor's response to mechanical stimuli is explored via cyclic loading tests in various loading conditions. The sensor's durability is investigated via long-term cyclic loading tests. Finally, the piezoresistive mechanism of the sensor's response is studied via in situ micro-strain testing under SEM. This chapter addresses research objectives iii and iv per section 1.4 of CHAPTER 1.

4.2. Experimental

4.2.1. Characterization of piezoresistive sensors under cyclic compressive loads

To establish the PDMS/MWCNT sensor's response to mechanical stimuli, cyclic compression tests were carried out. An Instron 5969 Column Universal Testing Machine was employed in this task. The PDMS/MWCNT sensor was sandwiched between two insulated copper plates attached on parallel plate test fixtures. Wires were soldered to the copper plates and connected to leads of an Agilent 34401A multimeter to collect the resistance of the sample throughout the cyclic tests. The test setup is the same as that used in CHAPTER 3, shown in Figure 21. The sensor was first tested to characterize its compression sensing range by applying cyclic compression strains of 1%, 2%, 3%, 4%, 5%, 10%, 15%, and 20% at a constant crosshead rate of 1 mm/min while collecting resistance data. The sensor's piezoresistive response dependence on

strain rate was investigated via cyclic compression loading at a max compression strain of 5% with strain rates of 1%, 10%, 100%, and 500%/min. The electrical resistance of the sensor was recorded throughout all tests. To investigate the effect of fatigue on the PDMS/MWCNT compression sensor, a long-term durability test was performed. The sample was clamped between two copper plates into the same testing setup mentioned previously. The sensor underwent cyclic compression at 5% compressive strain with a constant strain rate of 10%/min for 500 cycles while collecting resistance data. The resulting resistance response was used to characterize the sensor's durability and robustness for longer term use under cyclic loading.

4.2.2. Characterization of piezoresistive sensing mechanism

To investigate the PDMS/MWCNT sensor's sensing mechanism, in situ compression testing was performed under an SEM. The compression sensor was cut vertically down the middle and sputter coated with gold palladium to increase its conductivity and avoid charging under SEM. The compression sensor was then clamped into a micro-strain testing stage and placed into an SEM, as shown in Figure 29. The sensor surface was imaged before and after loading to compare the nanomorphology between the two mechanical states before and after the compressive load is applied. Images were taken at two locations on the sensor, one near the top and the other one near the bottom, to visualize the movement, reorganization, and reorientation of the MWCNT networks. The piezoresistive sensing mechanism was investigated by observing the reorganization of MWCNT network before and after loading, via the SEM images.

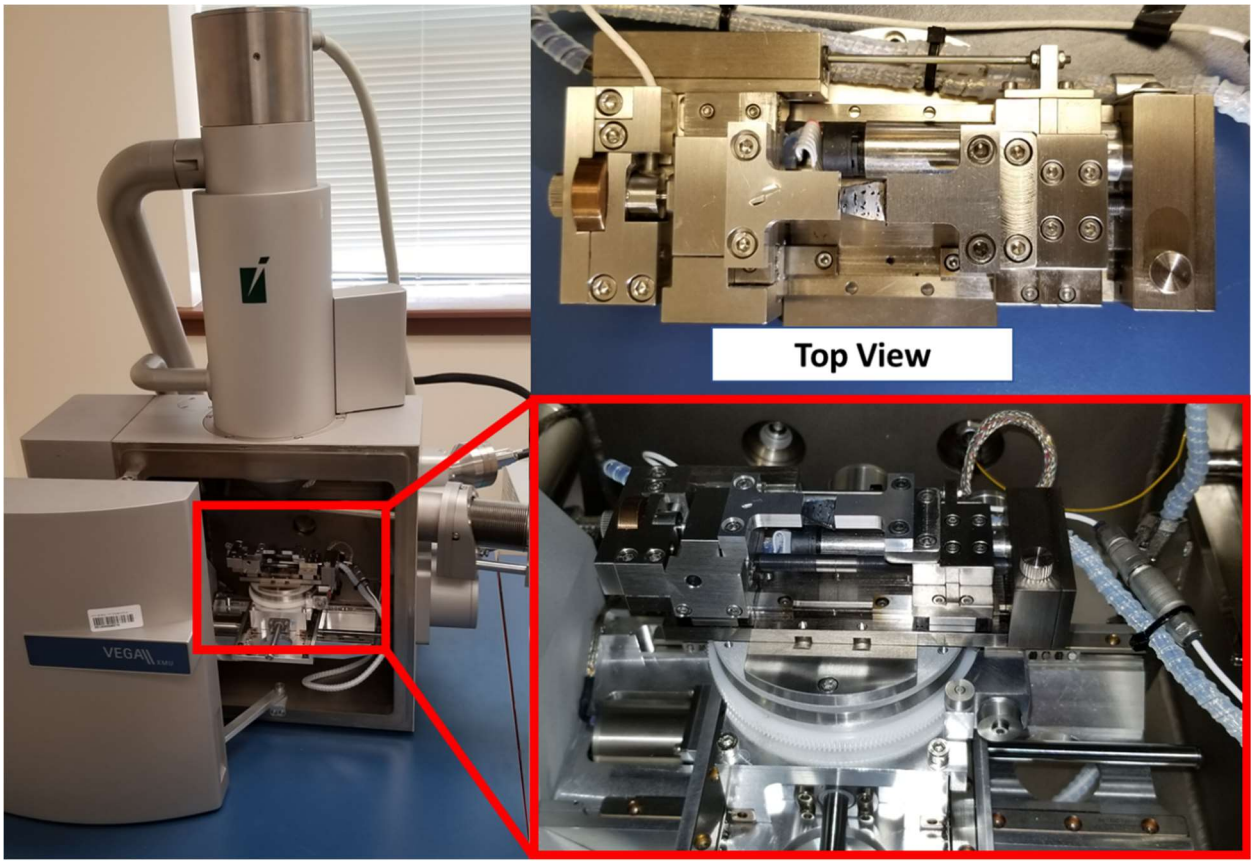

Figure 29. Experimental setup for in situ micro-strain testing SEM imaging [49].

4.3. Results

4.3.1. Microscale morphology of MWCNTs in nanocomposites

To gain insight into the MWCNT dispersion and internal morphology of the PDMS/MWCNT compression sensor, the sensor's cross section along the loading direction was imaged in an SEM. No MWCNT agglomerates were identified during the SEM imaging. Four SEM images of the sensor's cross section, imaged at 20 kV, are shown in Figure 30(a) to (d). It is expected that the sensor's performance will improve with the level of dispersion. Higher dispersion results in a larger number of individual MWCNT being spread throughout the polymer matrix, increasing the possibility of formation of MWCNT networks, thus resulting in a decrease in the electrical

resistance of the sensor. A common way to characterize the performance of a sensor is to study its relative resistance change, given by equation (4).

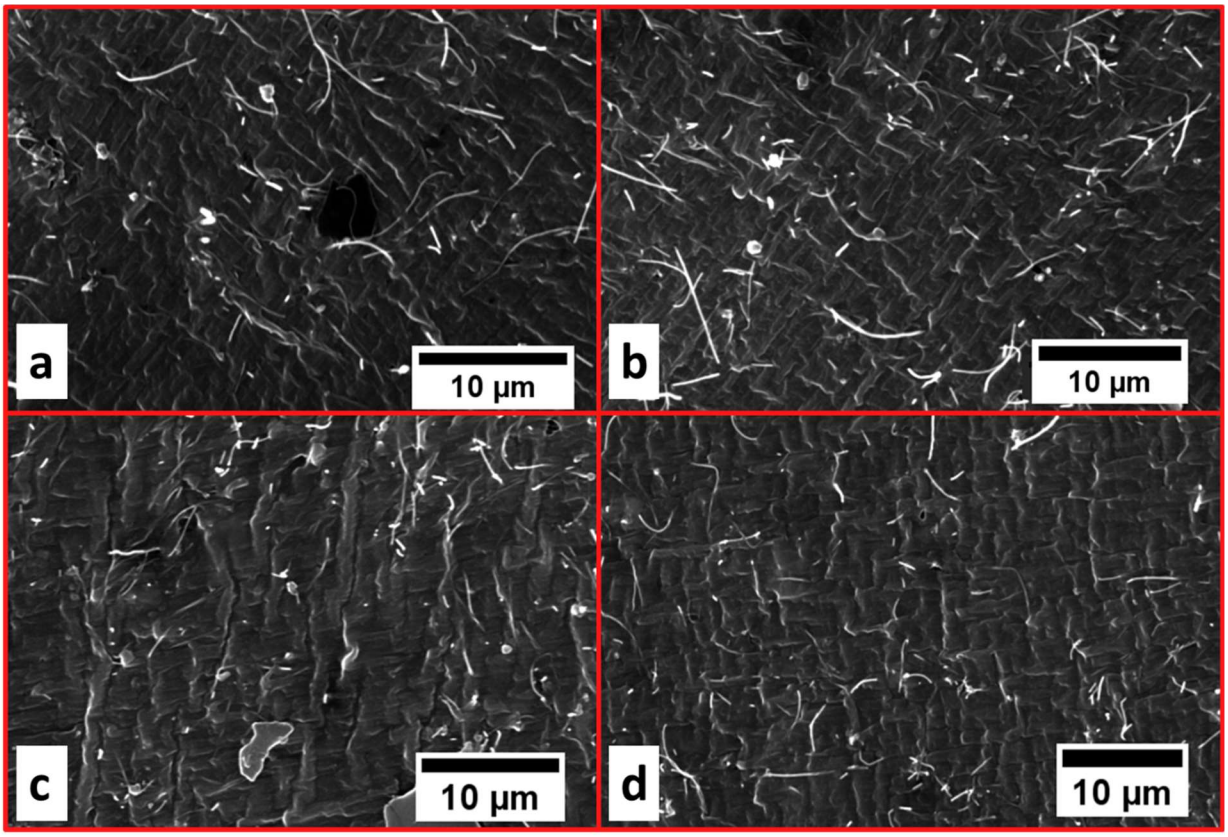

Figure 30. SEM images of PDMS/MWCNT compression sensor cross-section at four locations (magnification of 28803 in (a) and (c), and magnification of 20003 in (b) and (d)).

4.3.2. Piezoresistive sensing under compressive loads

The compression sensors were subjected to compressive maximum strains of 1%, 2%, 3%, 4%, 5%, 10%, 15%, and 20% with a constant crosshead speed of 1 mm/min to Relative resistance change results for cyclic testing at maximum strains of 1%, 3%, 5%, 10%, and 15% are shown in Figure 31(a) along with their corresponding strain at all points in Figure 31(b). Five cycles of compression and release loading are shown for each maximum strain. Figure 31(a) shows that

while the applied strain increased, the resistance of the sensor decreased. The resistance response was highly repeatable, as exemplified by the almost identical response from cycle to cycle at each max strain. The sensor's response was sensitive to the applied strain during, both, the loading and unloading phases of load application, showing increasing resistance change with increase in compression strain. Resistance decreases by about 24%, 55%, 73%, 86%, and 90% for the 1%, 3%, 5%, 10%, and 15% strains, respectively. At max strains of 10% and higher, as the sensor approached the point of the maximum strain, the resistance quickly reversed and began to increase, forming a peak at the point of highest strain. This hysteresis effect has not been well understood and could be caused by multiple factors, including reconfiguration of the electro-conductive percolating channels, a breakdown of the conductive network, and relaxation and elongation of the PDMS base material. Similar hysteresis has been reported in other piezoresistance based nanocomposite sensors that utilize carbon black and graphene nanoparticles to form the conductive network [55, 56]. In the case of elastomer-based sensors, this was especially important as these materials had relatively high Poisson's ratios (0.45–0.50 for PDMS [9]). As the PDMS/MWCNT sensor was compressed, MWCNTs translated, rotated, and bent, creating new electrical networks and decreasing the overall electrical resistance. However, as the PDMS elastomer was subjected to higher strains, MWCNT networks began to saturate, and further strain could cause damage to the electrical networks. Furthermore, another piezoelectric effect causing this artificial resistance peak could be attributed to the lateral expansion of the material due to its Poisson's ratio, effectively increasing the distance between adjacent networks and possibly causing a breakdown of electrical pathways.

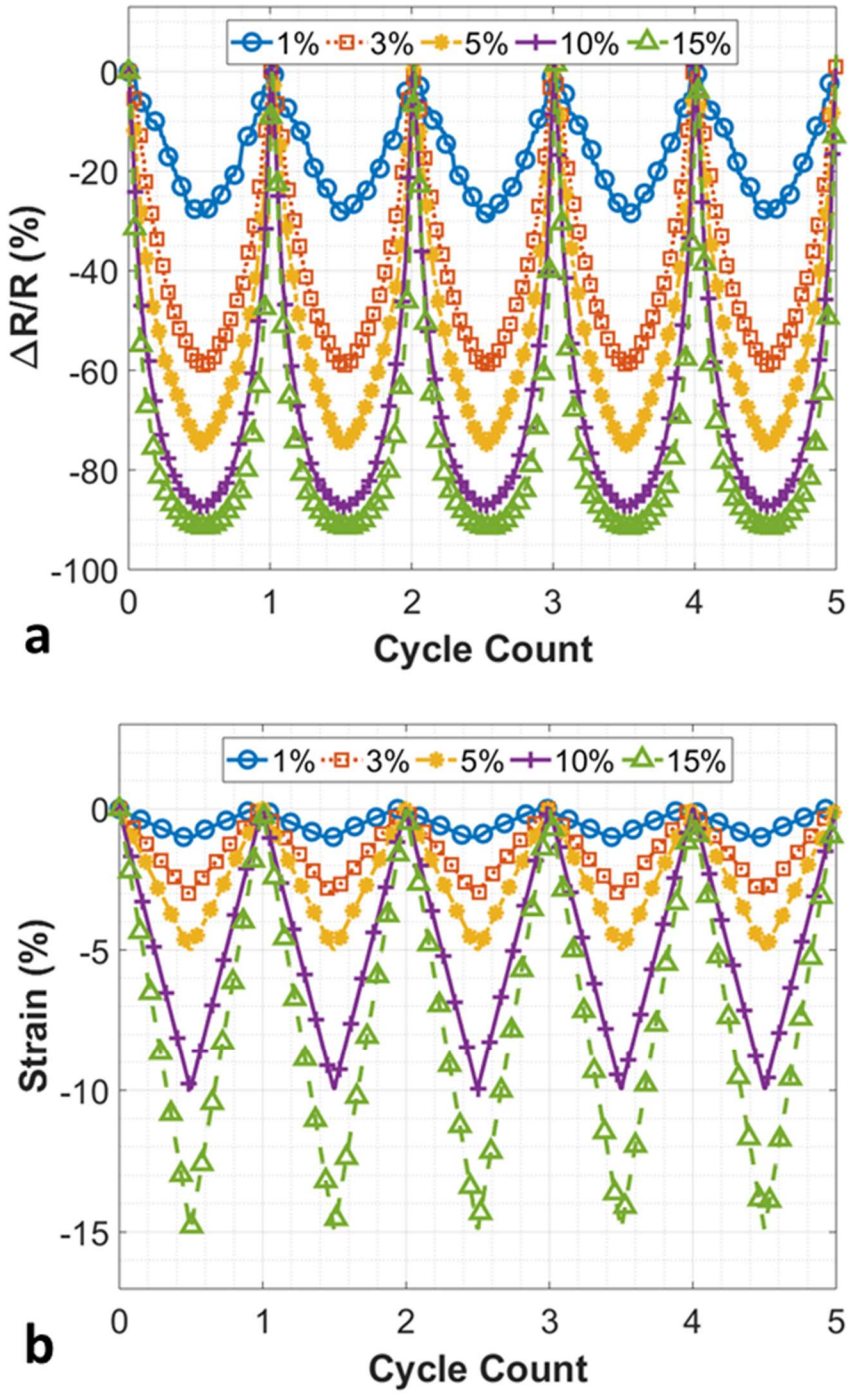

Figure 31. Cyclic strain testing at various max strains, holding crosshead speed constant: (a) relative resistance change versus cycle count and (b) applied strain versus cycle count.

A quantitative approach to characterize the sensitivity of a compression sensor is via its relative resistance change normalized by the applied strain, better known as gauge factor. Gauge factor is calculated via equation (5). Figure 32(a) and (b) show the resulting GF and ΔR/R values at different max strains. As the applied strain increases, the GF value also decreased with a seemingly asymptotic behavior as it reaches the highest max strains applied in this study. Likewise, although the relative resistance change increased with increasing max strain, it rose asymptotically. A gauge factor of 24 was observed at max strains of 1%, decreasing all the way down to about 4.6 for max strains of 20%. For comparison, gauge factors between 1.38 and 12.4 have been reported in the literature for PDMS/MWCNT compression sensors [18]. However, the higher gauge factors in the literature were achieved at much higher weight loadings, upward of 18 wt%. Therefore, the compression sensor reported in this work, with a MWCNT weight concentration of 1.5%, is more cost-effective.

Moreover, to place the sensor's response in the context of pressure, the stress vs strain and stress vs ΔR/R curve are shown in Figure 33a and Figure 33b, respectively. The stress displays linear behavior up to 5% strain, after which it deviates, but remains almost linear to 20% strain/360 kPa. The sensing response shows a large variation, as the sensing results are linear up until about 75% resistance change, before rising to 85% (about 10% strain), and then going to infinity as the stress rises above 360 kPa. Combined with the results shown in Figure 32, it can be concluded that the optimal sensing performance of this sensor is up to 10% strain. Due to the ease of manufacturing, however, this is not an issue since sensor geometry can be changed to accommodate the application.

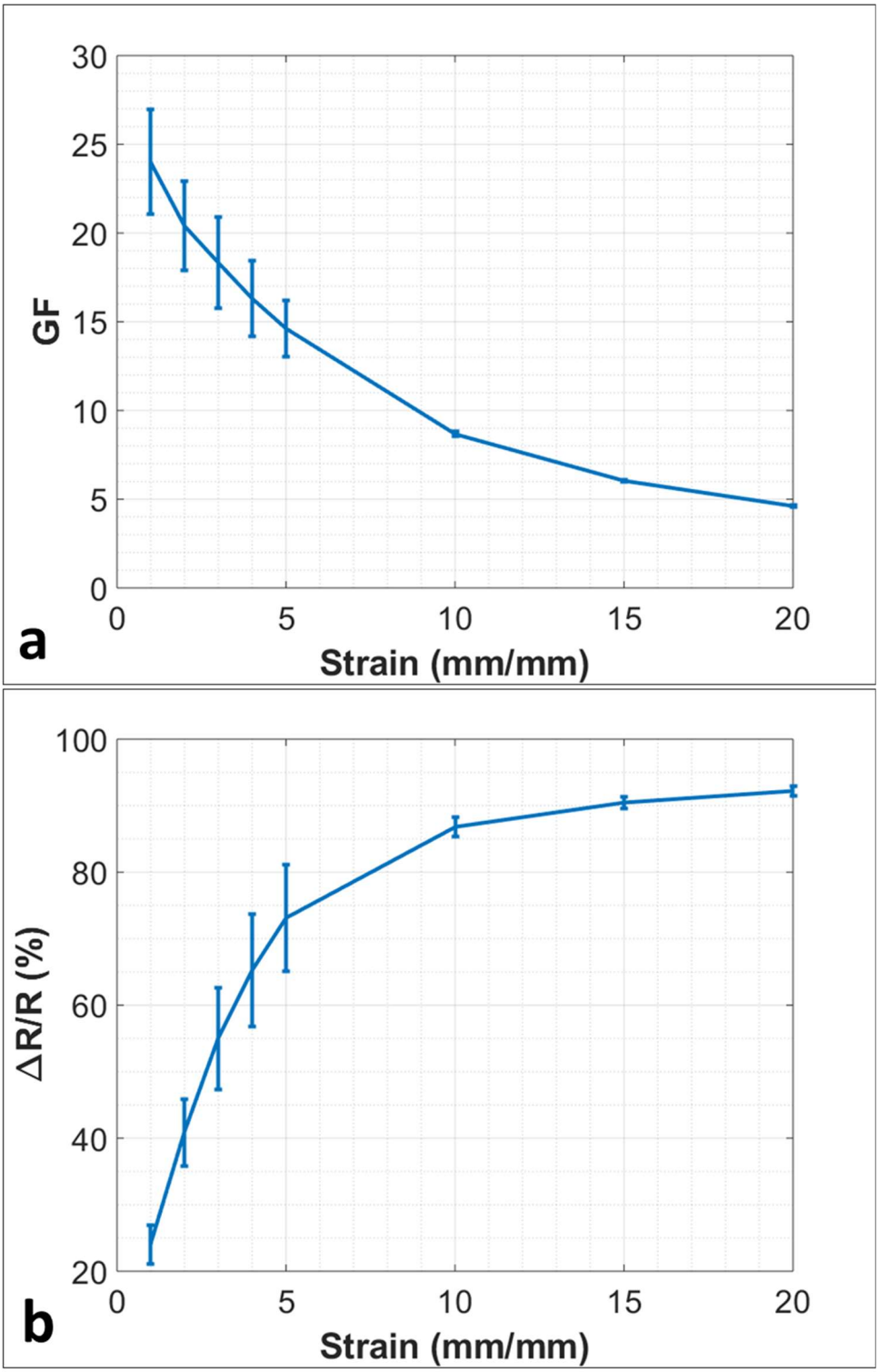

Figure 32. (a) Gauge factor and (b) ΔR/R versus strain based on cyclic loading at various max strains.

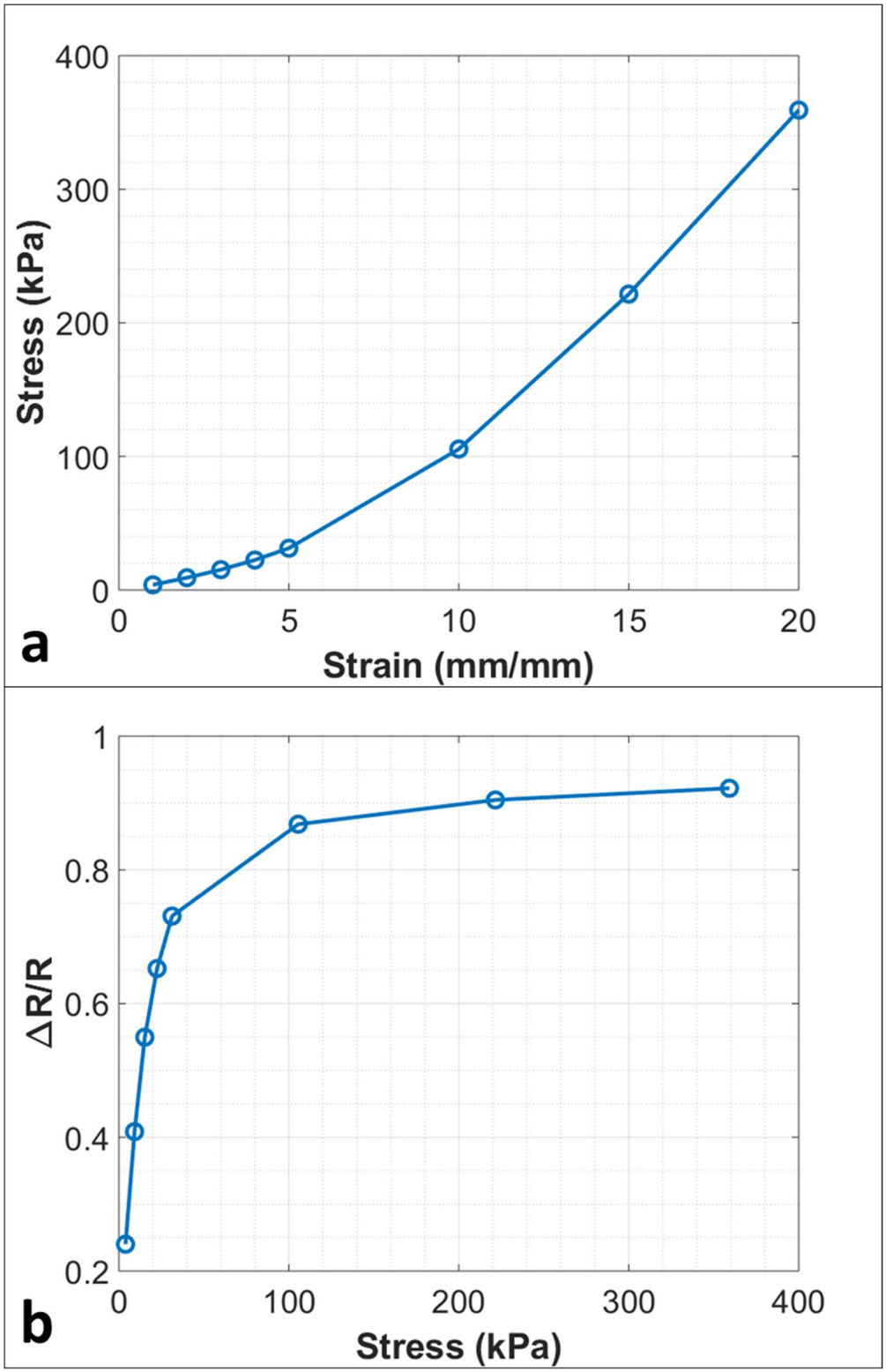

Figure 33(a) Stress vs strain and (b)ΔR/R vs strain for the 3D printed sensor.

The PDMS/MWCNT sensor's dependence on strain rate was investigated to validate its versatility. The sensor was subjected to cyclic loading with a max strain of 5% at strain rates of 1%, 10%, 100%, and 500%/min. The piezoresistive response of five cycles at various strain rates is shown in Figure 34a and the summary of the strain rate results is shown in Figure 34b. The response of the sensor at the varying strain rates was almost identical, with overlapping curves in the loading and unloading phases of the test. The results indicated that the PDMS/MWCNT compression sensors, along with their high sensitivity at low strains, are highly versatile in applications where load rate sensitivity may not be known during design. It should be noted that as the strain rate of the sensor increased, a minor deviation of the sensor's response occurred. At the end of the loading phase, the sensor's resistance dropped further with increasing strain rate. As shown in the summarized results (Figure 34b), the material's resistance changed increased slightly with increasing strain rate up until a rate of 50%/min. However, as shown in Figure 34a, the material quickly recovered and returned to its original resistance along the same curve for all strain rates.

To evaluate its robustness, the 3D printed compression sensor was subjected to a long-term durability test. The PDMS/MWCNT compressions sensor was subjected to a cyclic strain of 5% at a constant strain rate of 0.10/min for 500 cycles. Figure 35b summarizes the results of the durability test, plotting five cycles of the relative resistance change at representative point throughout the test, while Figure 35a shows the entire cyclic durability test. The sensor's resistance response was at its highest point during the first 100 cycles, exhibiting about a 5% drop in relative resistance change between the first and second 100 cycles. However, after this decrease, the sensor's response was consistent and did not change for the remaining 400 cycles. To study the effect of cyclic loading on material's piezoresistive response during the durability test, the pressure

versus strain was plotted ever 100 cycles, starting with cycle 1 (Figure 36). The PDMS/MWCNT nanocomposite showed no effects to its mechanical behavior as a result of long-term cyclic loading. Cycle 1 closely matched with cycle 500, proving the durability of the presented 3D printed sensors.

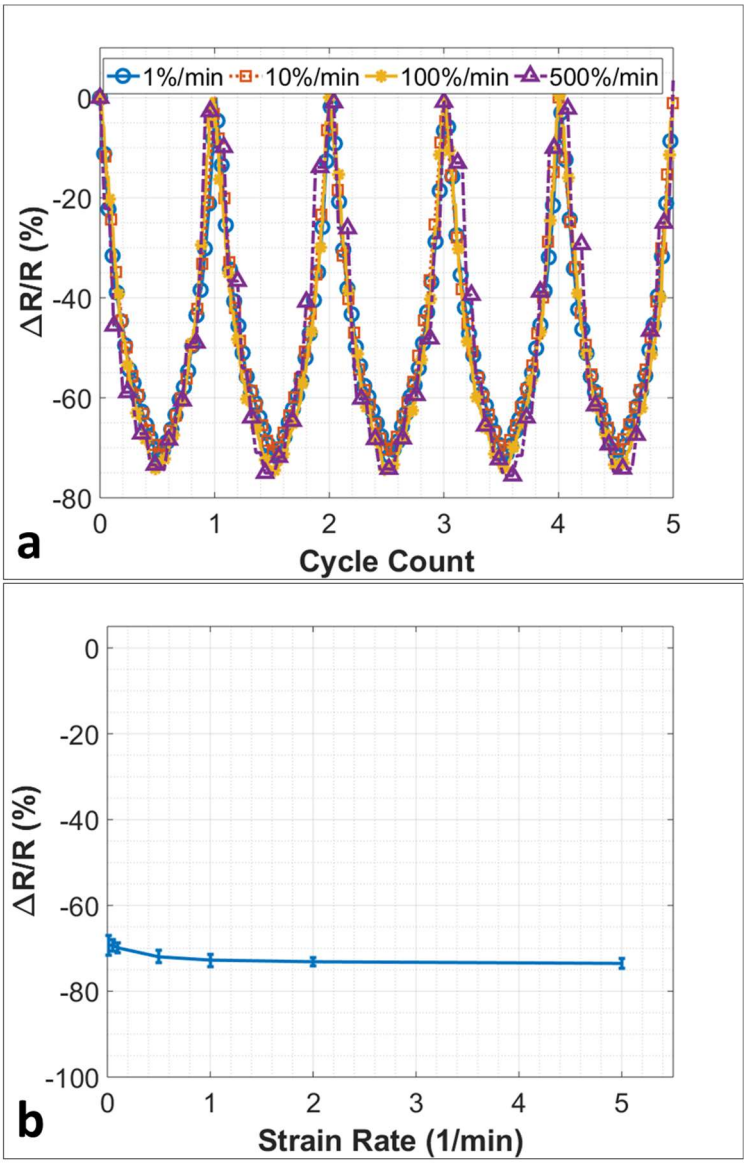

Figure 34. Relative resistance change results for cyclic loading at varying strain rates – (a) cyclic and (b) summarized results.

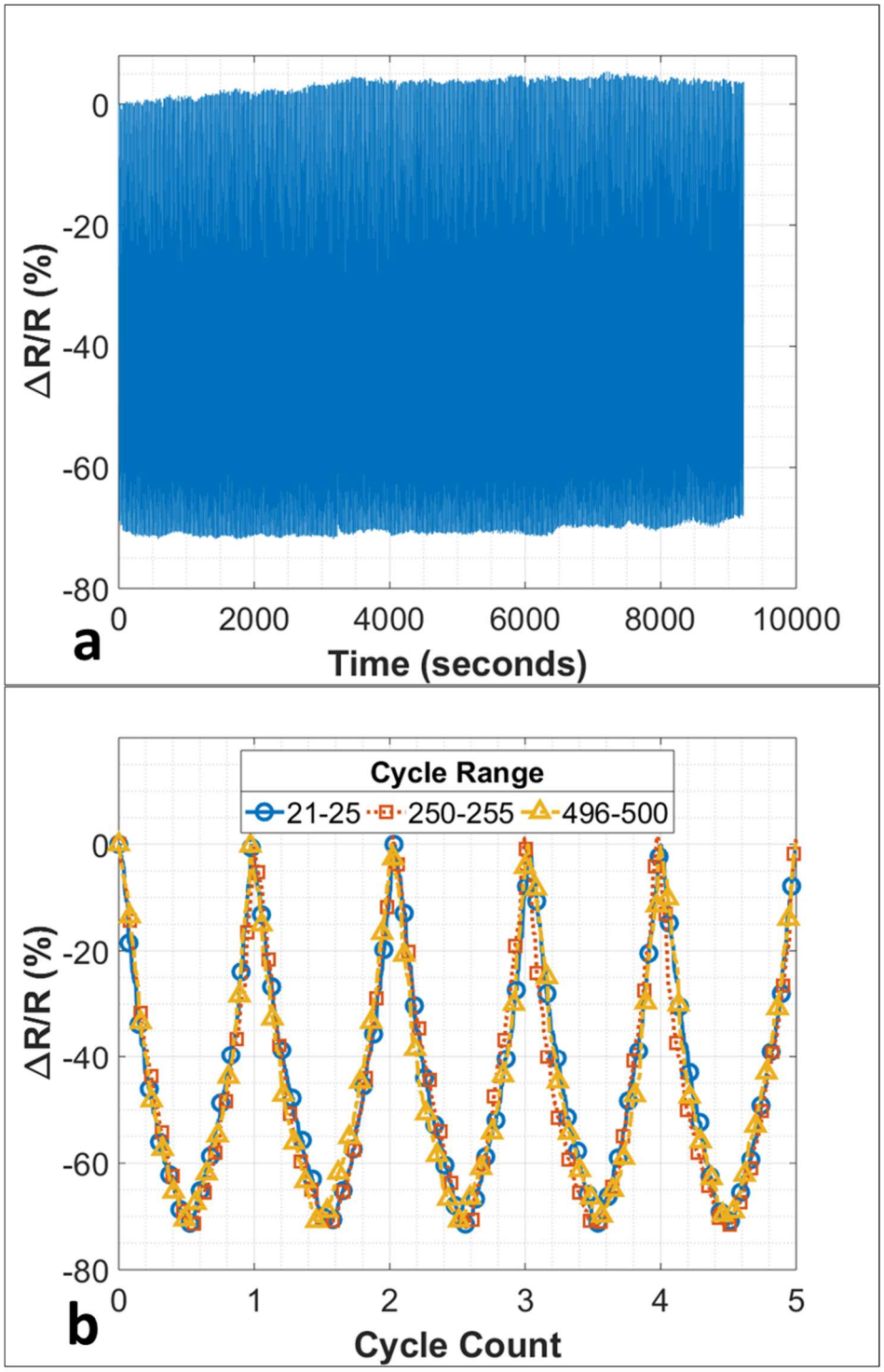

Figure 35. Relative resistance change for (a) the durability test and (b) 5 representative cycles at various phases in the test.

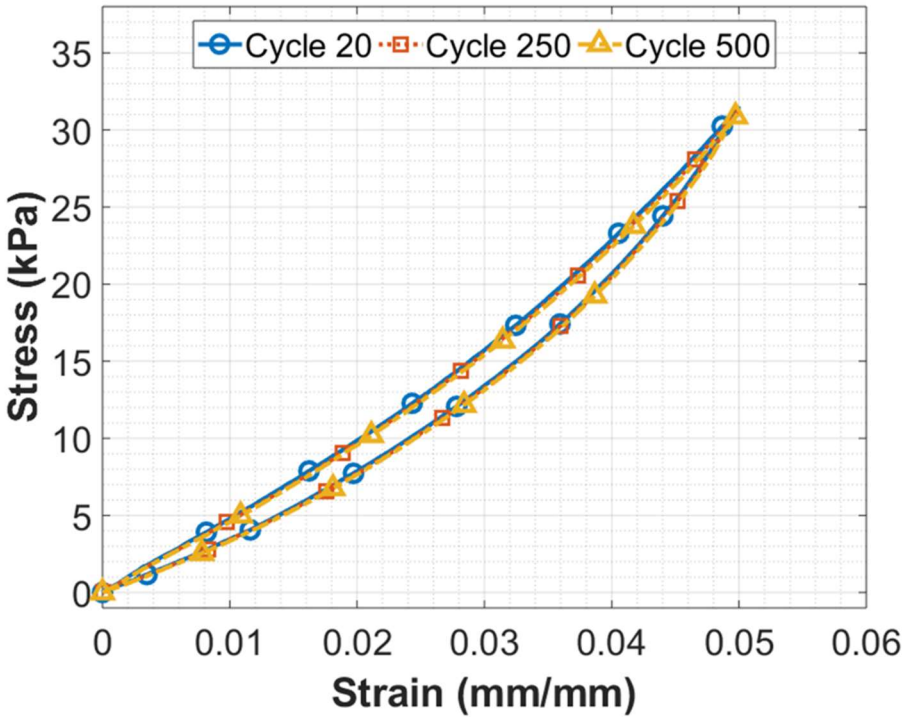

Figure 36. Stress versus strain curve at 3 representative cycles of the durability test.

4.3.3. Characterization of piezoresistive sensing mechanism

To observe the piezoresistive mechanism of the 3D printed PDMS/MWCNT compression sensor, in situ micromechanical tests were performed within an SEM to show the morphological reorganization of MWCNT conductive network under external loads. The piezoresistive mechanism in strain and compression sensors is due to the reorganization of the nanofillers within the polymer under mechanical deformation. This piezoresistive sensing phenomenon has been simulated and modeled in the literature [57, 58]. Four contributions to this effect have been investigated in published modeling efforts: strain induced CNT deformation, contact and tunneling resistance, strain-induced CNT reorientation, and electrical properties of pristine CNTs. However, to the best of our knowledge, detailed experimental validation and characterization of the piezoresistive sensing mechanism has not been well reported using in situ mechanical testing and

visualization methods. To address this point, the sensor was mounted in a compressive testing stage and inserted into an SEM chamber for imaging. Figure 37 shows SEM images of the cross section of the compression sensor before (Figure 37(a)) and after (Figure 37(b)) loading, imaged at 20 kV and a magnification of 20003. In these SEM images, compressive load was applied horizontally. Polymer realignment was observed in Figure 37(b) via the vertical lines throughout the image. Several areas in the images have been highlighted to visualize the MWCNT's reorganization, reorientation, and bending under compressive load. Comparing areas 1a and 1b confirms that MWCNTs experienced bending under loading which led to the restructuring of electrical networks. Area 2a shows two sets of intersecting nanotubes with a distance of about 3 mm. After loading, the distance between these two sets of intersecting MWCNTs decreased to 1.94 um. This supports the theory that conductive fillers move closer under compressive loading, thereby forming new conducting pathways and decreasing the material's electrical resistance via the tunneling effect. Areas 3, 4, 5, and 6 showed the reorientation of nanotubes prior to and after loading. The cumulative effects of MWCNT reorganization within the entire polymer matrix controlled the piezoresistive response of the sensor.

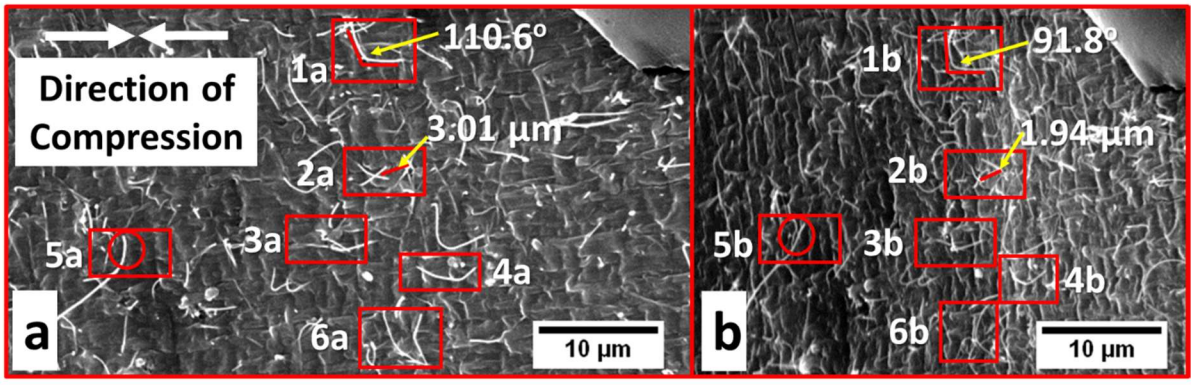

Figure 37. SEM images of in situ micromechanical tests before (a) and after (b) application of compressive load.

4.4. Conclusion

In this chapter, a PDMS/MWCNT compression sensor was developed and characterized. The sensor was 3D printed vertically, layer by layer, using a modified commercial 3D printer. The internal morphology of the sensor was imaged via SEM to characterize the dispersion of the MWCNTs. The compression sensor's electrical performance was investigated via cyclic compressive strain testing at seven different max strains, showing excellent piezoresistive response at strains up to 15%. The sensor's response to loading and unloading was linear. The sensor showed excellent sensitivity at a variety of strains, displaying a gauge factor of about 16 at 1% max strain, and a gauge factor of about 5 at 15% max strain. The sensor's versatility was tested via cyclic loading at five different strain rates, holding the max strain constant. The sensor showed almost identical resistance response under varying strain rates. Finally, the sensor's piezoresistive mechanism was visualized via in situ micromechanical testing under SEM imaging. The reorganization and reorientation of the MWCNTs was visualized, confirming excellent dispersion achieved during fabrication as well as the restructuring of the internal conductive networks under compressive loading. The results show sensor's high sensitivity and versatile load range sensing, making it an excellent choice in applications where loading rate is either variable or unknown.

CHAPTER 5. CONCLUSION AND FUTURE WORK

This work investigated the use of 3D printing to fabricate compression sensors from a thermosetting PDMS/CNT nanocomposite. PDMS/CNT inks with 1.0 – 3.0 wt% CNT content were synthesized using a hybrid sonication/magnetic mixing method. Pristine PDMS is a flowing polymer, and thus has no yield point. To 3D print this polymer, it is important to study the effects of CNT to its rheology to assess whether this material can be used for additive manufacturing. Oscillatory rheological tests revealed that polymer inks containing CNT content of 1.5 wt% or higher possessed a yield point. Thus, 8x8x8 mm cube samples were 3D printed using PDMS/CNT inks with 1.5-3.0 wt% CNT in two 3D printing patters: aligned rectilinear and concentric. Similar samples were cast using all inks synthesized for this work. Density cup measurements were used to calculate the porosity of the 3D printed specimen to understand potential process induced pore formation. Increasing CNT content in the nanocomposite was found to directly increase the resulting porosity of the 3D printed part. In addition, resistivity and conductivity measurements were taken of all 3D printed and cast samples to explore the effects of 3D printing and 3D printing pattern on the resulting electrical properties of the final geometry. It was found that, as expected, conductivity increased and resistivity decreased with increasing CNT content. Moreover, the percolation curve of the 3D printed samples closely matched that of the cast, and little difference was found between the electrical properties of the samples fabricated with the rectilinear and concentric 3D printing pattern. From these experiments, it was concluded that the optimal PDMS/CNT ink was that with 1.5 wt% CNT. Its low porosity, yield point, and relatively high resistivity make it an ideal candidate for 3D printing of piezoresistive sensors. This ink was used for the remainder of the study.

With the 3D printing ink selected, the effects of 3D printed parameters on the piezoresistive performance of the final geometry were explored. To assess their piezoresistive response, each sample underwent cyclic compressive loading at 10% strain and a crosshead speed of 1 mm/min. Testing both the rectilinear and concentric printed cubes in all 3 axes revealed that the 3D printed samples displayed isotropic properties, and lacked the alignment in the filament deposition direction discussed in other studies. Moreover, piezoresistive response comparison with the cast samples revealed that both the rectilinear and concentric printed cubes displayed similar resistance change as the cast sample. This quantitatively proves 3D printing as a viable alternative for fabricating compression. To further explore the effect of the additive manufacturing process on the fabricated sensors, two 3D printing parameters were explored: nozzle needle size and printing speed. Samples were printed using a 410 μm needle at printing speeds of 1, 2, 4, and 8 mm/s. Likewise, samples were printed at 1 mm/s using nozzle needle sizes of 410, 710, and 1400 μm. All samples produced very similar resistance change, proving that 3D printing is not only a viable source of fabricating nanocomposite based sensors, but that the process parameters can be changed without affecting the piezoresistive performance of the end product.

Having optimized the ink and explored processing parameters, cubic compression sensors were 3D printed using a PDMS/CNT nanocomposite ink with 1.5 wt% CNT. The 3D printhead speed was set to 1mm/s and the nozzle needle size was 410 μm. High mag SEM images of the cross section of the samples reveal satisfactory nanofiller dispersion, with no agglomerates. Cyclic loading tests at 1% - 20% compressive strain with a constant crosshead speed of 1mm/min were performed to fully characterize the piezoresistive response of the samples. This test revealed that increasing strain increased the resistance change, approaching an asymptote at 20% strain. A particularly high gauge factor of 24 was measured at 1% strain. To explore the effect of loading

rate on the piezoresistive performance of the printed sensor, cyclic testing was performed at a constant max strain of 5% with strain rates of 1%-500%/min. Results reveal that resistance change from all strain rates closely matched, proving the versatility of the printed sensors. To explore the robustness of the sensors, a durability test at 5% with a strain rate of 10%/min for 500 cycles was performed. The sample showed little degradation from the first cycles to the last, with no detectable change to mechanical properties. Finally, the piezoresistive mechanism of the 3D printed sensor was validated via in-situ micromechanical testing under SEM. Images revealed CNT network reorganization due to CNT movement within the matrix material, likely inducing tunneling effect which reduce the material's resistance.

This work details the development and exploration of 3D printed nanocomposite PDMS/CNT compression sensors. The value of this work is that it proves that 3D printing is a viable replacement to casting of sensors fabricated from thermosetting nanocomposites. Moreover, because 3D printing parameters were found to have no influence on the piezoresistive performance of the printed sensors, this process can be tailored to fit the needs of the user, allowing to focus on geometry accuracy or high output. In addition, although this study showed the fabrication of monolithic sensors, because no anisotropic behavior was detected as a result of 3D printed, this fabrication method is highly valuable for sensors of complex geometry where complex molds do not have to be repeatedly made and edited. Similarly, this process allows for the facile prototyping of complex geometries for iterative design, saving the waste of mold materials.

Although this work experimentally demonstrates the feasibility of the application of additive manufacturing to thermosetting nanocomposites, it is far from a comprehensive study as it explores one representative case. This work should serve as a starting point to continue to generalize this procedure. To this end, several points can be expanded on to do so. To capture a fully defined

model, it is first important to understand the interactions between the nozzle and material, before the material even touches the substrate. In this regard, a computational model should be developed that corelates the complex shear forces on the flowing polymer by the nozzle to pressure from the syringe plunger pushes the material out. Once this is done, we can extract more detailed polymer flow data for each individual polymer desired for printing, and the rheological tests performed can be better informed. Continuing, this representative fluid flow model from the syringe could be used to understand the immediate alignment of nanofillers at the print nozzle and, along with the rheological properties of the printed polymer, can be used to understand the long-term diffusion based alignment disturbance phenomenon that occurs once the polymer is deposited, prior to curing.

REFERENCES

[1] "Methods and technologies for the implementation of large-scale robot tactile sensors," *IEEE Trans. Robot.,* vol. 27, p. 389, 2011.

[2] I. Kang, M. J. Schulz, J. H. Kim, V. Shanov, and D. Shi, "A carbon nanotube strain sensor for structural health monitoring," *Smart materials and structures,* vol. 15, no. 3, p. 737, 2006.

[3] "Highly stretchy black gold e-skin nanopatches as highly sensitive wearable biomedical sensors," *Adv. Electron. Mater.,* vol. 1, p. 1, 2015.

[4] T. Yamada *et al.*, "A stretchable carbon nanotube strain sensor for human-motion detection," *Nature nanotechnology,* vol. 6, no. 5, p. 296, 2011.

[5] F. Avilés, A. I. Oliva-Avilés, and M. Cen-Puc, "Piezoresistivity, Strain, and Damage Self-Sensing of Polymer Composites Filled with Carbon Nanostructures," *Advanced Engineering Materials,* vol. 20, no. 7, p. 1701159, 2018.

[6] E. Sollier, C. Murray, P. Maoddi, and D. Di Carlo, "Rapid prototyping polymers for microfluidic devices and high pressure injections," *Lab on a Chip,* 10.1039/C1LC20514E vol. 11, no. 22, pp. 3752-3765, 2011.

[7] K. F. Lei, K.-F. Lee, and M.-Y. Lee, "Development of a flexible PDMS capacitive pressure sensor for plantar pressure measurement," *Microelectronic Engineering,* vol. 99, pp. 1-5, 2012/11/01/ 2012.

[8] K. Khanafer, A. Duprey, M. Schlicht, and R. Berguer, "Effects of strain rate, mixing ratio, and stress–strain definition on the mechanical behavior of the polydimethylsiloxane (PDMS) material as related to its biological applications," *Biomedical Microdevices,* journal article vol. 11, no. 2, p. 503, December 05 2008.

[9] I. D. Johnston, D. K. McCluskey, C. K. L. Tan, and M. C. Tracey, "Mechanical characterization of bulk Sylgard 184 for microfluidics and microengineering," *Journal of Micromechanics and Microengineering,* vol. 24, no. 3, p. 035017, 2014/02/28 2014.

[10] S. C. B. Mannsfeld *et al.*, "Highly sensitive flexible pressure sensors with microstructured rubber dielectric layers," *Nature Materials,* Article vol. 9, p. 859, 09/12/online 2010.

[11] J. F. Christ, N. Aliheidari, A. Ameli, and P. Pötschke, "3D printed highly elastic strain sensors of multiwalled carbon nanotube/thermoplastic polyurethane nanocomposites," *Materials & Design,* vol. 131, pp. 394-401, 2017.

[12] M. Abshirini, M. Charara, Y. Liu, M. Saha, and M. C. Altan, "3D Printing of Highly Stretchable Strain Sensors Based on Carbon Nanotube Nanocomposites," *Advanced Engineering Materials,* vol. 20, no. 10, p. 1800425, 2018.

[13] C. Li, E. T. Thostenson, and T.-W. Chou, "Dominant role of tunneling resistance in the electrical conductivity of carbon nanotube–based composites," *Applied Physics Letters,* vol. 91, no. 22, p. 223114, 2007.

[14] N. Hu, Y. Karube, C. Yan, Z. Masuda, and H. Fukunaga, "Tunneling effect in a polymer/carbon nanotube nanocomposite strain sensor," *Acta Materialia,* vol. 56, no. 13, pp. 2929-2936, 2008.

[15] W. Luheng, D. Tianhuai, and W. Peng, "Influence of carbon black concentration on piezoresistivity for carbon-black-filled silicone rubber composite," *Carbon,* vol. 47, no. 14, pp. 3151-3157, 2009/11/01/ 2009.

[16] M. G. King, A. J. Baragwanath, M. C. Rosamond, D. Wood, and A. J. Gallant, "Porous PDMS force sensitive resistors," *Procedia Chemistry,* vol. 1, no. 1, pp. 568-571, 2009/09/01/ 2009.

[17] L. Miao, B. Amine, and L. Yi-Kuen, "Fabrication technology of piezoresistive conductive PDMS for micro fingerprint sensors," in *2007 IEEE 20th International Conference on Micro Electro Mechanical Systems (MEMS)*, 2007, pp. 251-254.

[18] L. Junyong, L. Miao, A. Bermak, and L. Yi-Kuen, "Study of piezoresistance effect of carbon nanotube-PDMS composite materials for nanosensors," in *2007 7th IEEE Conference on Nanotechnology (IEEE NANO)*, 2007, pp. 1240-1243.

[19] K. S. Novoselov *et al.*, "Electric Field Effect in Atomically Thin Carbon Films," *Science,* vol. 306, no. 5696, pp. 666-669, 2004.

[20] H.-B. Yao *et al.*, "A Flexible and Highly Pressure-Sensitive Graphene–Polyurethane Sponge Based on Fractured Microstructure Design," *Advanced Materials,* vol. 25, no. 46, pp. 6692-6698, 2013.

[21] B. Zhu *et al.*, "Microstructured Graphene Arrays for Highly Sensitive Flexible Tactile Sensors," *Small,* vol. 10, no. 18, pp. 3625-3631, 2014.

[22] L.-Q. Tao *et al.*, "Graphene-Paper Pressure Sensor for Detecting Human Motions," *ACS Nano,* vol. 11, no. 9, pp. 8790-8795, 2017/09/26 2017.

[23] L.-C. Tang *et al.*, "The effect of graphene dispersion on the mechanical properties of graphene/epoxy composites," *Carbon,* vol. 60, pp. 16-27, 2013/08/01/ 2013.

[24] S. Iijima, "Helical microtubules of graphitic carbon," *Nature,* vol. 354, no. 6348, pp. 56-58, 1991/11/01 1991.

[25] N. Hu *et al.*, "Investigation on sensitivity of a polymer/carbon nanotube composite strain sensor," *Carbon,* vol. 48, no. 3, pp. 680-687, 2010/03/01/ 2010.

[26] Z.-M. Dang, M.-J. Jiang, D. Xie, S.-H. Yao, L.-Q. Zhang, and J. Bai, "Supersensitive linear piezoresistive property in carbon nanotubes⁄silicone rubber nanocomposites," *Journal of Applied Physics,* vol. 104, no. 2, p. 024114, 2008.

[27] J. Hwang *et al.*, "Poly(3-hexylthiophene) wrapped carbon nanotube/poly(dimethylsiloxane) composites for use in finger-sensing piezoresistive pressure sensors," *Carbon,* vol. 49, no. 1, pp. 106-110, 2011/01/01/ 2011.

[28] S. Pegel, P. Pötschke, G. Petzold, I. Alig, S. M. Dudkin, and D. Lellinger, "Dispersion, agglomeration, and network formation of multiwalled carbon nanotubes in polycarbonate melts," *Polymer,* vol. 49, no. 4, pp. 974-984, 2008/02/18/ 2008.

[29] J. Hwang *et al.*, "Poly (3-hexylthiophene) wrapped carbon nanotube/poly (dimethylsiloxane) composites for use in finger-sensing piezoresistive pressure sensors," *Carbon,* vol. 49, no. 1, pp. 106-110, 2011.

[30] P. Pötschke, T. D. Fornes, and D. R. Paul, "Rheological behavior of multiwalled carbon nanotube/polycarbonate composites," *Polymer,* vol. 43, no. 11, pp. 3247-3255, 2002/05/01/ 2002.

[31] B. Gorissen, E. Milana, D. Reynaerts, and M. D. Voider, "Lithographic production of vertically aligned CNT strain sensors for integration in soft robotic microactuators," in *2018 IEEE International Conference on Soft Robotics (RoboSoft)*, 2018, pp. 400-405.

[32] W. Luo, M. Charara, M. C. Saha, and Y. Liu, "Fabrication and characterization of porous CNF/PDMS nanocomposites for sensing applications," *Applied Nanoscience,* journal article January 23 2019.

[33] M. Charara, W. Luo, M. C. Saha, and Y. Liu, "Investigation of Lightweight and Flexible Carbon Nanofiber/Poly Dimethylsiloxane Nanocomposite Sponge for Piezoresistive Sensor Application," *Advanced Engineering Materials,* vol. 0, no. 0, p. 1801068.

[34] W. Lee, H. Oh, J. Huh, and S. J. Moon, "Simple CNT nanocomposite piezoresistive press sensor," in *2017 International Conference on Information and Communication Technology Convergence (ICTC)*, 2017, pp. 1041-1043.

[35] J. T. Muth *et al.*, "Embedded 3D Printing of Strain Sensors within Highly Stretchable Elastomers," *Advanced Materials,* vol. 26, no. 36, pp. 6307-6312, 2014.

[36] B. Gorissen, C. Van Hoof, D. Reynaerts, and M. De Volder, "SU8 etch mask for patterning PDMS and its application to flexible fluidic microactuators," *Microsystems &Amp; Nanoengineering,* Article vol. 2, p. 16045, 09/12/online 2016.

[37] Q. Sun, G. M. Rizvi, C. T. Bellehumeur, and P. Gu, "Effect of processing conditions on the bonding quality of FDM polymer filaments," *Rapid Prototyping Journal,* vol. 14, no. 2, pp. 72-80, 2008.

[38] P. Tran, T. D. Ngo, A. Ghazlan, and D. Hui, "Bimaterial 3D printing and numerical analysis of bio-inspired composite structures under in-plane and transverse loadings," *Composites Part B: Engineering,* vol. 108, pp. 210-223, 2017/01/01/ 2017.

[39] R. Melnikova, A. Ehrmann, and K. Finsterbusch, "3D printing of textile-based structures by Fused Deposition Modelling (FDM) with different polymer materials," *IOP Conference Series: Materials Science and Engineering,* vol. 62, p. 012018, 2014/08/08 2014.

[40] B. Caulfield, P. E. McHugh, and S. Lohfeld, "Dependence of mechanical properties of polyamide components on build parameters in the SLS process," *Journal of Materials Processing Technology,* vol. 182, no. 1, pp. 477-488, 2007/02/02/ 2007.

[41] T. J. Hinton, A. Hudson, K. Pusch, A. Lee, and A. W. Feinberg, "3D Printing PDMS Elastomer in a Hydrophilic Support Bath via Freeform Reversible Embedding," *ACS Biomaterials Science & Engineering,* vol. 2, no. 10, pp. 1781-1786, 2016/10/10 2016.

[42] T. J. Hinton *et al.*, "Three-dimensional printing of complex biological structures by freeform reversible embedding of suspended hydrogels," *Science Advances,* vol. 1, no. 9, 2015.

[43] V. Ozbolat, M. Dey, B. Ayan, A. Povilianskas, M. C. Demirel, and I. T. Ozbolat, "3D Printing of PDMS Improves Its Mechanical and Cell Adhesion Properties," *ACS Biomaterials Science & Engineering,* vol. 4, no. 2, pp. 682-693, 2018/02/12 2018.

[44] S.-Z. Guo, K. Qiu, F. Meng, S. H. Park, and M. C. McAlpine, "3D Printed Stretchable Tactile Sensors," *Advanced Materials,* vol. 29, no. 27, p. 1701218, 2017.

[45] A. K. Grosskopf, R. L. Truby, H. Kim, A. Perazzo, J. A. Lewis, and H. A. Stone, "Viscoplastic Matrix Materials for Embedded 3D Printing," *ACS Applied Materials & Interfaces,* vol. 10, no. 27, pp. 23353-23361, 2018/07/11 2018.

[46] S. Waheed *et al.*, "3D printed microfluidic devices: enablers and barriers," *Lab on a Chip,* 10.1039/C6LC00284F vol. 16, no. 11, pp. 1993-2013, 2016.

[47] M. Abshirini, M. Charara, Y. Liu, M. C. Saha, and M. C. Altan, "Additive Manufacturing of Polymer Nanocomposites With In-Situ Strain Sensing Capability," no. 52170, p. V012T11A007, 2018.

[48] T. Bhattacharjee *et al.*, "Writing in the granular gel medium," *Science Advances,* vol. 1, no. 8, p. e1500655, 2015.

[49] M. Charara, M. Abshirini, M. C. Saha, M. C. Altan, and Y. Liu, "Highly sensitive compression sensors using three-dimensional printed polydimethylsiloxane/carbon nanotube nanocomposites," *Journal of Intelligent Material Systems and Structures,* vol. 0, no. 0, p. 1045389X19835953.

[50] A. D. Valentine *et al.*, "Hybrid 3D Printing of Soft Electronics," *Advanced Materials,* vol. 29, no. 40, p. 1703817, 2017.

[51] A. Sydney Gladman, E. A. Matsumoto, R. G. Nuzzo, L. Mahadevan, and J. A. Lewis, "Biomimetic 4D printing," *Nature Materials,* vol. 15, p. 413, 01/25/online 2016.

[52] B. G. Compton and J. A. Lewis, "3D-Printing of Lightweight Cellular Composites," *Advanced Materials,* vol. 26, no. 34, pp. 5930-5935, 2014.

[53] J. E. Smay, J. Cesarano, and J. A. Lewis, "Colloidal Inks for Directed Assembly of 3-D Periodic Structures," *Langmuir,* vol. 18, no. 14, pp. 5429-5437, 2002/07/01 2002.

[54] M. Abshirini, M. Charara, P. Marashizadeh, M. C. Saha, M. C. Altan, and Y. Liu, "Functional nanocomposites for 3D printing of stretchable and wearable sensors," *Applied Nanoscience,* journal article April 17 2019.

[55] K. Yamaguchi, J. J. C. Busfield, and A. G. Thomas, "Electrical and mechanical behavior of filled elastomers. I. The effect of strain," *Journal of Polymer Science Part B: Polymer Physics,* vol. 41, no. 17, pp. 2079-2089, 2003.

[56] R. Zhang *et al.*, "Strain sensing behaviour of elastomeric composite films containing carbon nanotubes under cyclic loading," *Composites Science and Technology,* vol. 74, pp. 1-5, 2013.

[57] W. S. Bao, S. A. Meguid, Z. H. Zhu, and G. J. Weng, "Tunneling resistance and its effect on the electrical conductivity of carbon nanotube nanocomposites," *Journal of Applied Physics,* vol. 111, no. 9, p. 093726, 2012.

[58] S. Gong and Z. H. Zhu, "On the mechanism of piezoresistivity of carbon nanotube polymer composites," *Polymer,* vol. 55, no. 16, pp. 4136-4149, 2014/08/05/ 2014.